



2nd Advanced Optical Metrology Compendium

Advanced Optical Metrology

Geoscience | Corrosion | Particles | Additive Manufacturing: Metallurgy, Cut Analysis & Porosity



EVIDENT
OLYMPUS

WILEY

The latest eBook from **Advanced Optical Metrology**.
Download for free.

This compendium includes a collection of optical metrology papers, a repository of teaching materials, and instructions on how to publish scientific achievements.

With the aim of improving communication between fundamental research and industrial applications in the field of optical metrology we have collected and organized existing information and made it more accessible and useful for researchers and practitioners.

EVIDENT
OLYMPUS

WILEY

Unravelling the Origin of Ultra-Low Conductivity in SrTiO₃ Thin Films: Sr Vacancies and Ti on A-Sites Cause Fermi Level Pinning

Maximilian Morgenbesser, Alexander Viernstein, Alexander Schmid,*
Christopher Herzig, Markus Kubicek, Stefanie Taibl, Gesara Bimashofer, Jochen Stahn,
Carlos Antonio Fernandes Vaz, Max Döbeli, Federico Biautti, Juan de Dios Sirvent,
Maciej Oskar Liedke, Maik Butterling, Michał Kamiński, Martin Tolkiehn, Vedran Vonk,
Andreas Stierle, Andreas Wagner, Albert Tarancon, Andreas Limbeck, and Jürgen Fleig

Different SrTiO₃ thin films are investigated to unravel the nature of ultra-low conductivities recently found in SrTiO₃ films prepared by pulsed laser deposition. Impedance spectroscopy reveals electronically pseudo-intrinsic conductivities for a broad range of different dopants (Fe, Al, Ni) and partly high dopant concentrations up to several percent. Using inductively-coupled plasma optical emission spectroscopy and reciprocal space mapping, a severe Sr deficiency is found and positron annihilation lifetime spectroscopy revealed Sr vacancies as predominant point defects. From synchrotron-based X-ray standing wave and X-ray absorption spectroscopy measurements, a change in site occupation is deduced for Fe-doped SrTiO₃ films, accompanied by a change in the dopant type. Based on these experiments, a model is deduced, which explains the almost ubiquitous pseudo-intrinsic conductivity of these films. Sr deficiency is suggested as key driver by introducing Sr vacancies and causing site changes (Fe_{Sr} and Ti_{Sr}) to accommodate nonstoichiometry. Sr vacancies act as mid-gap acceptor states, pinning the Fermi level, provided that additional donor states (most probably Ti_{Sr}²⁺) are present. Defect chemical modeling revealed that such a Fermi level pinning also causes a self-limitation of the Ti site change and leads to a very robust pseudo-intrinsic situation, irrespective of Sr/Ti ratios and doping.

1. Introduction

The electrochemical bulk properties of SrTiO₃ have been thoroughly investigated and different bulk defect models are available for doped and undoped SrTiO₃.^[1,2] These models are well in line with the conductivities found experimentally at different temperatures and oxygen partial pressures. Therefore, SrTiO₃ often serves as a model material for other perovskite-type titanates (e.g., BaTiO₃, Pb(Zr,Ti)O₃),^[3] since its bulk properties and bulk defect concentrations are so well understood. SrTiO₃ is a mixed conductor,^[3] enabling a tailoring of the conductivity from predominantly electronic (via electrons or electron holes) to ionic (via oxygen vacancies), depending on temperature and oxygen partial pressure.^[1,4,5]

Another way of tuning the conductivity of SrTiO₃ is the introduction of dopant elements. Donor doping can be achieved by trivalent ions on the A-site (e.g., La³⁺) or pentavalent ions on the B-site (e.g., Nb⁵⁺).

M. Morgenbesser, A. Viernstein, A. Schmid, C. Herzig, M. Kubicek,
S. Taibl, A. Limbeck, J. Fleig
Institute of Chemical Technologies and Analytics
Getreidemarkt 9, TU Wien, 1060 Vienna, Austria
E-mail: alexander.e164.schmid@tuwien.ac.at

G. Bimashofer, J. Stahn, C. A. F. Vaz
Laboratory for Neutron Scattering and Imaging
Paul Scherrer Institut
Villigen PSI, 5232 Villigen, Switzerland

 The ORCID identification number(s) for the author(s) of this article can be found under <https://doi.org/10.1002/adfm.202202226>.

© 2022 The Authors. Advanced Functional Materials published by Wiley-VCH GmbH. This is an open access article under the terms of the Creative Commons Attribution License, which permits use, distribution and reproduction in any medium, provided the original work is properly cited.

DOI: 10.1002/adfm.202202226

G. Bimashofer
Department of Chemistry and Applied Biosciences
ETH Zürich
Rämistrasse 101, 8092 Zurich, Switzerland

C. A. F. Vaz
Swiss Light Source
Paul Scherrer Institut
Forschungsstrasse 111, Villigen-PSI, CH-5232 Villigen, Switzerland

M. Döbeli
Laboratory of Ion Beam Physics
ETH Zürich
Otto-Stern-Weg 5, HPK H31, 8093 Zürich, Switzerland

F. Biautti, J. de Dios Sirvent, A. Tarancon
Catalonia Institute for Energy Research (IREC)
Jardins de les Dones de Negre 1, 2^a pl., Sant Adrià del Besòs
08930 Barcelona, Spain

M. O. Liedke, M. Butterling, A. Wagner
Institute of Radiation Physics
Helmholtz-Zentrum Dresden-Rossendorf
Bautzner Landstraße 400, 01328 Dresden, Germany

In those cases, cation vacancies or electrons compensate the charge. Acceptor dopants in SrTiO₃ are monovalent ions on the A-site (e.g., K⁺) or trivalent ions on the B-site (e.g., Fe³⁺). In such p-type SrTiO₃, the charge is compensated by oxygen vacancies or electron holes. Also, co-doping (e.g., Sr_{1-x}La_xTi_{1-y}Cr_yO₃) is possible and allows to change the optical, catalytic, and electrochemical properties of SrTiO₃ for different purposes.^[6,7] Furthermore, the existence of trivalent “magic dopants” (e.g., Mn³⁺) is reported in literature,^[8] acting simultaneously as a donor and as an acceptor, depending on the site occupation, which is in line with a self-compensation mechanism suggested in theoretical studies for trivalent dopants.^[9] For other dopant elements including chromium,^[10] erbium,^[11] magnesium,^[12] and rhodium,^[13,14] both A- and B-site occupation are discussed as well. In addition, Ti on the A-site was reported for SrTiO₃.^[15–18] Please note that the change in site occupation for Ti⁴⁺ from the B-site (Ti_B^x) to the A-site (Ti_A^x) is accompanied by the introduction of donor states.

Vacancies strongly influence the defect equilibria of SrTiO₃ and, thus, change the conductivity. While the direct influence of oxygen vacancies as charge carriers on the conductivity is easily accessible via ionic conductivity, the impact of their cation counterparts (i.e., cation vacancies) is less clear. In many experiments, cation vacancies are considered immobile due to the higher activation energy of cation motion.^[19] However, they can still affect the activation barrier of other defects (e.g., oxygen vacancies^[19–21]). Moreover, vacancies act as dopants, cation vacancies being acceptor dopants and oxygen vacancies being donor dopants,^[19,22–25] thereby strongly affecting the respective concentration of all other charge carriers and the properties of SrTiO₃. Additionally, cation stoichiometry might be also relevant at interfaces, for example, in the LaAlO₃/SrTiO₃ heterojunction.^[26]

The interplay between deliberate dopants and (often unintended) doping via cation nonstoichiometry has to be considered especially in the field of thin films, where cation nonstoichiometry is easily introduced during the deposition process.^[27–36] Thin films are becoming increasingly important, for example, for resistive switching^[37–44] and for various light induced phenomena^[45–50] in the emerging field of opto-ionics.^[51] SrTiO₃ thin films as well as other perovskite-type thin films are known to show a behavior different to their single or poly-crystalline counterparts.^[5,19,37,52,53] Structural differences (interfaces, strain, stress),^[54–56] dominating space charge zones,^[5,57] or nonstoichiometry accommodation^[19,29,58,59] in thin films have been discussed in literature and may explain deviating behavior. Even pseudo-intrinsic electronic conductivity was previously reported for Fe-doped SrTiO₃ thin films, meaning that a mid-gap Fermi level pinning leads to extremely low electron and hole concentrations in differently doped samples.^[37,52] A correlation with Sr stoichiometry was found,

indicating that this ultra low conductivity appears for substantial Sr vacancy concentrations.^[60]

In this study, numerous doped as well as undoped SrTiO₃ thin films were characterized via electrochemical impedance spectroscopy (EIS) with regard to their electrical conductivity. For various dopants (Fe, Ni, Al) and dopant concentrations (up to 10%), pseudo-intrinsic behavior with extremely low conductivities was found. To explain this outstanding thin film property, different additional characterization methods were employed, in order to determine the detailed elemental composition via inductively-coupled plasma optical emission spectroscopy (ICP-OES) and Rutherford back scattering spectrometry (RBS), film structure via X-ray diffraction (XRD) and X-ray standing wave (XSW) measurements, and defect chemistry via X-ray absorption spectroscopy (XAS) and positron annihilation lifetime spectroscopy (PALS). By combining all these pieces of information, a model is deduced explaining the ultra-low conductivity of many doped and undoped SrTiO₃ films. This model strongly suggests that similar phenomena may exist in many other large band gap multi-component thin films prepared by pulsed laser deposition.

2. Results

2.1. Conductivity Measurements

Doped and undoped SrTiO₃ thin films grown by pulsed laser deposition (PLD) were characterized via electrochemical impedance spectroscopy. Typical impedance spectra for several doping situations are plotted in **Figure 1**. The spectra for different thin films differ in the degree of distortion, from rather undistorted (e.g., 0.4% Ni-doped) to a rather pronounced distortion (e.g., 2% Fe-doped). The small low-frequency features found in some spectra are not further considered here. We can see in Figure 1 that the low frequency intercepts of the large arcs (R_{DC}) at ≈ 530 °C are rather similar (i.e., in the range of 180–280 k Ω) despite vastly different doping situations, from 0.4% to 5% dopant. (Please note the slightly different temperatures and film thicknesses; still the agreement of the resistances and of the 1426 Hz data point is surprising.) A detailed discussion of such impedance spectra of SrTiO₃ thin films is given elsewhere.^[60] Here, we give a brief summary of the main aspects deduced there: Since SrTiO₃ is an ionic and electronic conducting material, a transmission line model^[61–63] with ionic and electronic rails is appropriate for describing the spectra. Since the ionic conduction path is blocked at one or both electrodes, the DC resistance corresponds to the electronic resistance of the film and an electronic conductivity can be calculated from its value. This electronic conductivity is almost the same for all samples shown in Figure 1. Depending on the exact ionic conductivity and the chemical capacitance, however, additional features may appear in the spectra and give rise to the measured distortions of the arcs. Here, however, we focus on the electronic DC conductivity of the films.

The temperature dependent DC conductivity (i.e., electronic conductivity) of the 0.4% doped film is plotted in **Figure 2a**. Interestingly, this electronic conductivity is several orders of magnitude lower than the bulk values expected from literature

M. Kamiński, M. Tolkienn, V. Vonk, A. Stierle
Deutsches Elektronen Synchrotron (DESY)
Notkestraße 85, D-22607 Hamburg, Germany

A. Stierle
Fachbereich Physik
Universität Hamburg
22607 Hamburg, Germany

A. Tarancon
Catalan Institution for Research and Advanced Studies (ICREA)
08930 Barcelona, Spain

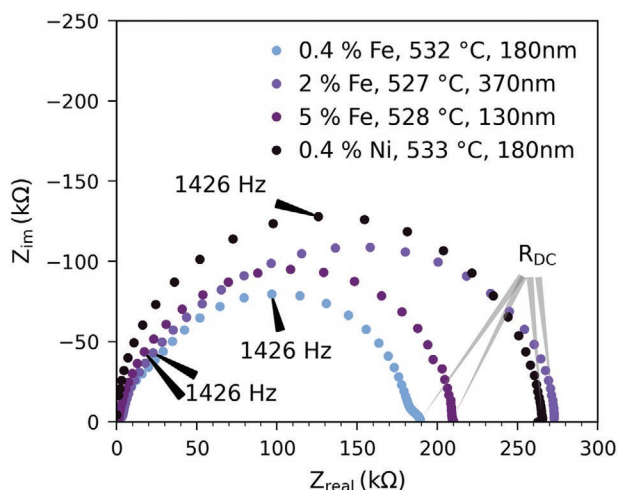


Figure 1. Electrochemical characterization of different SrTiO₃ thin films deposited from targets with 0.4%, 2%, and 5% Fe as well as 0.4% Ni doping. The measurement temperatures deviate slightly for the individual samples, but are all in the range of 527–533 °C. Film thicknesses are in the range of 130–370 nm. The DC resistances of the main arcs (R_{DC}) and the 1426 Hz data points are indicated for the different impedance spectra. The DC resistances are in the range of 180–280 kΩ. Different degrees of distortion can be identified, for example, nearly undistorted for 0.4% Ni to heavily distorted for 2% Fe doping.

for the respective compositions.^[37,64] In this figure, the conductivity is also compared with the electronic intrinsic conductivity of SrTiO₃ calculated from data sets in refs. [1, 2] by assuming a mid-gap Fermi level and thus equal hole and electron concentrations ($[h^+] = [e^-]$). These intrinsic electronic conductivities are very close or even up to a factor of four above the measured ultra-low conductivities. Due to this similarity we denote the measured conductivities as “pseudo-intrinsic.” Such low values were also reported in refs. [37, 60], but reasons are not understood so far. There must be a fundamental difference between SrTiO₃ bulk samples with acceptor-type bulk conductivity and the SrTiO₃ thin films with pseudo-intrinsic conductivity. This is further investigated and explained in the following.

Surprisingly, even a massive increase in doping concentration does not have a pronounced effect on the electronic DC conductivity for the Fe-doped SrTiO₃ thin films. This is plotted in Figure 2c for different Fe doping concentrations (0.4%, 1%, 2%, 5%, and 10%). For the sake of comparison, we also measured the conductivity of thin films deposited from a target with 30% Fe (STF73). The conductivity of a thin film deposited from a target containing 0.4% Fe doping is even independent of the oxygen partial pressure over a pressure range of five orders of magnitude (see Figure 2b), which is also in contrast to Fe-doped SrTiO₃ bulk samples.^[4] The conductivities of 30% Fe-doped SrTiO₃ films, on the other hand, are about five orders of magnitude higher at 350 °C, thus showing that we face a true thin film effect and not a measurement artifact.

Moreover, films deposited from nominally undoped SrTiO₃ as well as Ni-doped SrTiO₃ and Al-doped SrTiO₃ targets were measured (see Figure 2d) and the DC conductivities of all these thin films are again close to the calculated very low intrinsic conductivities, that is, $[h^+] = [e^-]$. Thus, for a vast number of

different films, neither the dopant concentration nor the dopant itself (Fe, Ni, Al) changes the conductivity, highlighting the very robust nature of this effect. We thus conclude that we do not face a special feature of a specific Fe-doped SrTiO₃ film, but an inherent property of many SrTiO₃ thin films deposited via PLD. Common defect models fail to explain such a conductivity behavior and to the best of the authors knowledge a mechanistic explanation was not proposed so far. However, a first hint was reported in a separate paper: When using highly off-stoichiometric PLD targets with 5 to 7% Sr excess, SrTiO₃ films result with “normal” conductivities (i.e., like for doped bulk samples rather than pseudo-intrinsic).^[60] This Sr excess in the target was shown to compensate substantial amounts of Sr vacancies otherwise present in the films.

This leads to the hypothesis that additional point defects present in our films, but not in bulk SrTiO₃, strongly reduce the electron and hole concentrations by a Fermi level pinning close to mid-gap, thus leading to the observed “pseudo-intrinsic” behavior. High defect concentrations in the films might also reduce the mobility of electrons and holes such that total conductivities even lower than nominal intrinsic conductivities are conceivable (cf., Figure 2) and almost intrinsic conductivities may indicate approximate but not necessarily exact mid-gap pinning of the Fermi level. In the following, we describe experimental results using several other methods, which give further information on the fundamental mechanism behind the pseudo-intrinsic behavior.

2.2. Chemical Analysis

The results for the chemical analysis are summarized in Table 1. Different SrTiO₃ thin films prepared from Fe-doped or Ni-doped to Al-doped or nominally undoped targets, were investigated using inductively-coupled plasma optical emission spectroscopy (ICP-OES). A more or less pronounced Sr deficiency, that is, a deviation of the Sr/(Ti+dopant) ratio from unity, is found for all thin films, mostly in the range of Sr/(Ti+X) = 0.90 (exception: Al doped SrTiO₃). Note that the dopant is attributed to the B-site in this consideration. The amount of dopant found in the samples also showed some deviations from the target compositions. Only a slight deviation was measured for a target with 1% Fe, where 0.9% Fe was measured in the thin film. Similarly, for a pellet with 10% Fe at the B-site, 8.7% Fe was found in the respective thin film. In case of the Ni-doped SrTiO₃, 1% Ni was found instead of the target concentration of 0.4% Ni. This is not a measurement artifact since the error for these measurements is usually well below 1% for the main components (Sr, Ti) and about 5% for the minor components, that is, dopants (e.g., 0.01 ± 0.0005). Different processes, including preferential scattering and incongruent ablation during pulsed laser deposition might lead to the discrepancy between the nominal and the experimentally found composition of such thin films.^[30,33,36,65] Similar stoichiometry differences are also reported for other materials, for example, LaMnO₃,^[66] La_{0.6}Ca_{0.4}MnO₃,^[67] La_{0.6}Sr_{0.4}MnO₃,^[68] Ca₃Co₄O₉,^[69] and SrMnO₃.^[70] Variation of the deposition parameters were often linked to the resulting thin film stoichiometry.^[29,58] A proper adjustment of these parameters may thus lead to

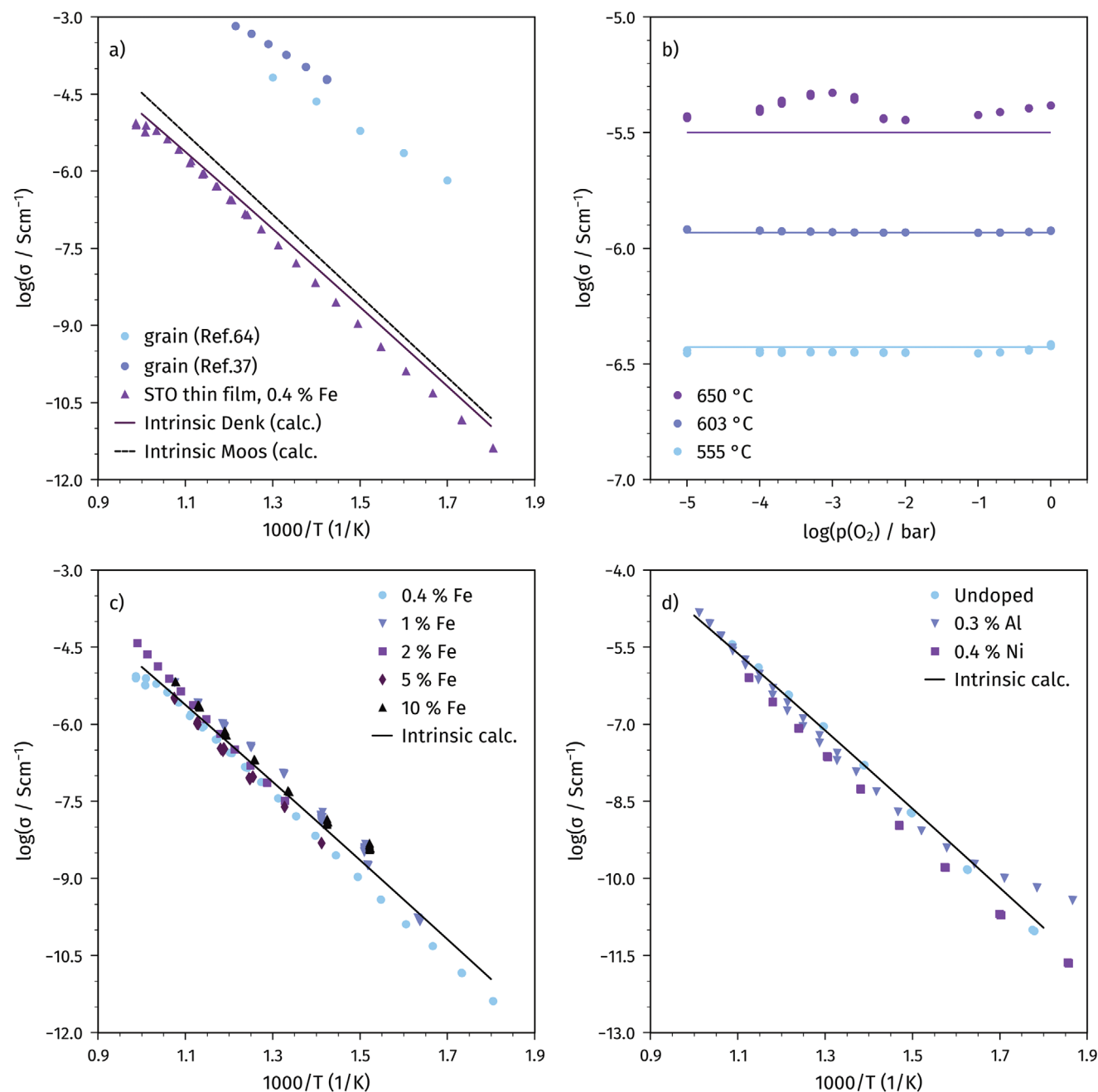


Figure 2. DC conductivity obtained from the DC resistance of doped SrTiO₃ thin films, measured by electrochemical impedance spectroscopy. a) Comparison of DC conductivities of thin films deposited from a 0.4% Fe doped target to the expected conductivity of bulk samples^[37,64] and to the calculated conductivity of pseudo-intrinsic electronic conductivity ($[h^{\bullet}] = [e^{\bullet}]$).^[1,2] b) oxygen partial pressure dependence of the conductivity of a Fe-doped thin film deposited from a target with 0.4% Fe at three different temperatures (555 °C, 603 °C and 650 °C). No variation of the conductivity is observed in an oxygen partial pressure range from 10^{-5} to 1 bar oxygen, the conductivity is close to the pseudo-intrinsic conductivity calculated from literature.^[1] c) DC conductivity of Fe-doped SrTiO₃ thin films deposited from targets with different doping concentrations ranging from 0.4% up to 10% together with the electronically intrinsic conductivity ($[h^{\bullet}] = [e^{\bullet}]$).^[1] d) DC conductivity of nominally undoped SrTiO₃ thin films and slightly acceptor doped thin films with different doping ions (Ni or Al).

stoichiometric films and thereby prevent the effects we describe here. In our specific case, some moderate changes of laser fluence and pulse frequency were performed, but turned out to be not sufficient to achieve fully stoichiometric films, while growth from targets with Sr excess yielded stoichiometric films.^[71]

The compositional results were confirmed by RBS. Here, a Fe doped SrTiO₃ thin film (with a nominal Fe content of 5% Fe at the B-site) on a SrTiO₃ substrate was investigated. Using RBS, a clear difference between the thin film and the substrate was found. This difference is attributed to a different Sr/Ti ratio

Table 1. Compositional analysis via inductively-coupled plasma optical emission spectroscopy (ICP-OES) and Rutherford back scattering spectroscopy/ time-of-flight heavy ion elastic recoil detection analysis (RBS/ToF-ERDA) of different SrTiO₃ thin films deposited from stoichiometric targets. The values are calculated for two cations per formula unit. Also the ratio between A-site cations (Sr) and supposed B-site cations (Ti, Fe, Ni, Al) is given (Sr/(Ti+X)). The relative error for these measurements is usually well below 1% for the main components (Sr, Ti) and about 5% for the minor components.

Target material	Thin film composition				Method
	Sr	Ti	Dopant	Sr/(Ti+X)	
SrTi _{0.99} Fe _{0.01} O ₃	0.950	1.041	0.009	0.905	ICP-OES
SrTi _{0.98} Fe _{0.02} O ₃	0.945	1.020	0.035	0.896	ICP-OES
SrTi _{0.95} Fe _{0.05} O ₃	0.937	1.015	0.048	0.881	RBS (Sr, Ti) ToF-ERDA (Fe)
SrTi _{0.9} Fe _{0.1} O ₃	0.960	0.953	0.087	0.923	ICP-OES
SrTi _{0.996} Ni _{0.004} O ₃	0.944	1.046	0.010	0.894	ICP-OES
SrTi _{0.997} Al _{0.003} O ₃	0.988	1.007	0.005	0.976	ICP-OES
SrTiO ₃	0.957	1.043		0.918	ICP-OES

of the thin film, compared to the substrate, although differences in the oxygen stoichiometry might also play a role. For the thin film, less Sr than Ti was found, whereas nominally less Ti would be expected. With RBS, the Fe content could not be determined reasonably because of the huge background from the Sr signal. The use of characteristic X-rays (PIXE) was excluded since the substrate material and the thin film are basically the same material, making it impossible to properly normalize the Fe X-ray yield to another element. Therefore, heavy ion elastic recoil detection analysis (ToF-ERDA) was performed. Here, a Fe/Ti ratio of 0.047 ± 0.005 was obtained, which is in line with the nominally expected value of 0.052, corresponding to a 5% dopant concentration at the B-site. Altogether, chemical analysis revealed Sr deficiency in all films. There are different ways for SrTiO₃ to accommodate this Sr deficiency, for example, via Sr vacancies in the lattice, segregation of Ti rich secondary phases (e.g., TiO₂) or anti-site defects (e.g., Ti_{Sr}²⁺).^[15–18] To resolve the predominant effect in our films, further film characterization was performed.

2.3. X-Ray Diffraction

In general, SrTiO₃ exhibits a cubic unit cell above $\approx 105\text{K}$.^[72,73] A cell parameter obtained from reciprocal space map (RSM) measurements was found to be $\approx 3.90 \text{ \AA}$, which is in line with literature data.^[74–76] However, the RSMs of the (002) reflections plotted in **Figure 3** show an elongated c cell parameter compared to the nominally undoped SrTiO₃ substrate for all deposited thin films except for the Al-doped layer. As a result, two separated diffraction peaks, one originating from the substrate and one from the thin film, can be seen. Further reflections, namely the (103) and the (113), were investigated. In each reciprocal space map of the (103) reflections (see S2, Supporting Information), again two reflections differing only in q_{\perp} can be seen (except for Al-doped SrTiO₃), confirming the enlarged c cell parameters found in most of the deposited thin films. A deviation of the in-plane cell parameters of the thin films from the substrate would result either in a shift in q_{\parallel} or in the intensities of the thin film peaks, which we did not observe.

To further address this issue, additional reciprocal space maps of the (113) reflections were measured (see S2, Supporting Information), showing shifts only in q_{\perp} direction (except for Al-doped SrTiO₃ exhibiting no shift at all). Please note that the Sr deficiency is also lower in Al-doped thin films compared to the other thin films, thus decreasing the difference in lattice parameter, as also observed in ref. [60] for similar cases.

No difference in the in-plane cell parameters can be found for any thin film compared to the single crystalline substrate. However, an elongation of the c cell parameter reduces the symmetry of the thin films and leads to a tetragonal lattice. The results of the recorded reciprocal space map are in line with literature data on SrTiO₃ thin films^[29,36,58] and are attributed to the existence of cation vacancies, that is, to films with a Sr/Ti ratio (or Sr/(Ti+dopant)) deviating from unity.^[77–79] Thus, we can conclude that at least part of the nominal Sr deficiency found in the chemical analysis is present in the form of Sr vacancies. This is also in agreement with high Sr vacancy concentration reported for SrTiO₃ films in literature.^[19]

2.4. Positron Annihilation Lifetime Spectroscopy

In **Figure 4a**, a nominally undoped SrTiO₃ thin film is characterized and compared with a nominally undoped SrTiO₃ single crystal. The dependence of the dominant component of the lifetime on implantation energies for the film on the substrate reflects a depth dependent change of the main ionic defect. Comparing the near surface signal of the film with the signal of the pure bulk sample reveals several differences. In the thin film, the predominant point defect is the Sr vacancy (lifetime: 281ps^[58]), which is in agreement with the chemical analysis (see Section 2.2) as well as the RSM data (see Section 2.3). In undoped single crystals the predominant cation vacancies seem to be titanium vacancies (lifetime: 189ps^[58]), see ref. [80] for a more detailed discussion of single crystals. The same trend can be observed for an iron doped SrTiO₃ thin film (deposited on Nb:SrTiO₃ and from a pellet with 2% Fe), see **Figure 4b**, where it is compared to an Fe-doped single crystal (0.15% Fe). Again, Sr vacancies are found in the thin film, while titanium

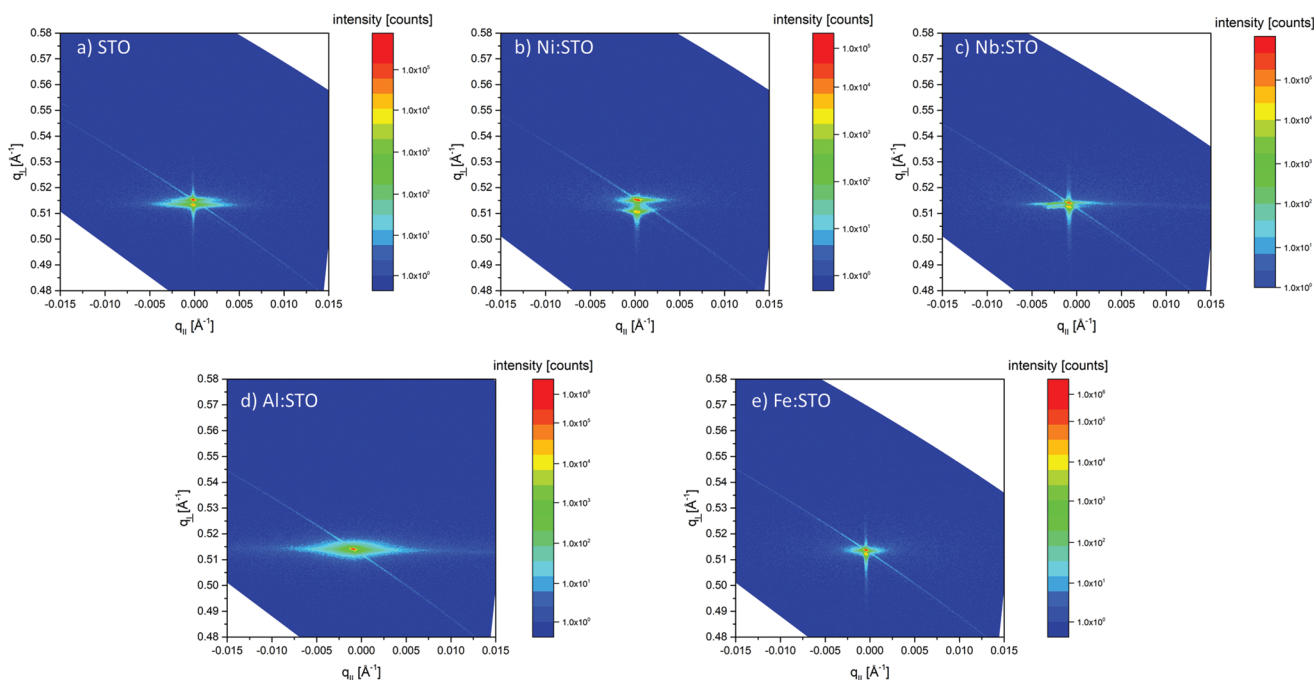


Figure 3. Structural characterization of different SrTiO₃ thin films on top of nominally undoped (001) oriented SrTiO₃ single crystals. a) Thin films were deposited from nominally undoped, b) 0.4% Ni-doped, c) 2% Nb-doped, d) 0.3% Al-doped, and e) 1% Fe-doped SrTiO₃ targets. Here, reciprocal space maps (RSM) for the (002) reflections are shown, revealing a severe deviation in the lattice parameter for the thin films compared to the underlying SrTiO₃ substrates. Except for the Al-doped thin film (d) the out of plane cell parameter *c* from each of the prepared thin films is elongated compared to the substrate. As a consequence, in the RSMs two separated reflexes can be found. The deviation between the thin film and the substrate can be attributed to cation vacancies. Taking the Sr deficiency found by elemental analysis into account, the cation vacancies are identified as Sr vacancies.

vacancies are present in the single crystal. The relative intensity I_{defect} for both undoped and Fe-doped films is close to 100%, which suggests large defect concentration and positron saturation trapping. In such a scenario positrons sense only the most affine defect type. In the case of single crystals, this component is absent and a shorter lifetime is found. When comparing the two single crystals, one observes a higher I_{defect} for the undoped crystal, indicating larger V_{Ti} concentration compared to the Fe-doped sample.

Taking into account the similar levels of Sr deficiency in the thin films (obtained from ICP-OES measurements in Section 2.2), Sr vacancies are probably also present in all the other thin films investigated. However, this does not mean that the Sr deficiency only leads to A-site vacancies. Rather, B-site ions on the A-site might reduce the A-site vacancy concentration compared to the nominal Sr-deficiency. Ti on the A-site was found or discussed in several studies. For example, Karjalainen et al. suggest that defects corresponding to positron lifetime of 185 ± 5 ps can be ascribed to Ti_{Sr} antisite.^[16] Another option is that the dopant, for example, Fe, occupies the A-site, which is considered next.

2.5. XSW

The XSW technique was used to determine whether Fe is located on interstitial, the A- and/or the B-sites. In **Figure 5a**, the normalized Fe K-fluorescence of the (002) Bragg reflection is shown as function of $(\Theta - \Theta_{\text{B}})$, with Θ the rocking angle and Θ_{B} the Bragg angle for the particular reflection, for a film

deposited from a target with 2% Fe and 5% Sr excess, corresponding to a stoichiometric thin film.^[60] The fluorescence yield exhibits a minimum at the low angle side of the Bragg position, followed by a maximum at the higher angle side. As expected for a bulk-like material, this means that the Fe is located at regular lattice sites and, down to the detection limit, no Fe at interstitials is found, see also the detailed simulations shown in Figure 9. The large peak in the fluorescence yield at $\Theta - \Theta_{\text{B}} = 0.01^\circ$ is caused by the strong and partially overlapping substrate reflection and does neither affect the analysis nor the interpretation. The period of the standing wave created by the (002) reflection was analyzed, see Section 5.

To differentiate between A- and B-site occupation of Fe, the (003) reflection can be used. The standing wave period of this reflection allows to differentiate between the regular A- and B-sites. Note that the (003) reflection is much weaker than (002) because scattering from the AO and BO₂ planes is out-of-phase, and thus the XSW signal level is lower. Here, we compare measurements on 2% Fe-doped films deposited from stoichiometric targets ($\text{SrTi}_{0.98}\text{Fe}_{0.02}\text{O}_3$) and from 5% Sr excess targets ($\text{Sr}_{1.05}\text{Ti}_{0.98}\text{Fe}_{0.02}\text{O}_3$). The simulations in Figure 5b show the change of the normalized fluorescence yield when the Fe occupancy changes from B-site only ($\xi = 0$) to A-site only ($\xi = 1$), with mixed occupation in between. The best agreement with the experimental data is obtained for $\xi = 0$ for the film grown with the 5% Sr excess target and when $\xi = 0.3-0.4$ for the film grown with the stoichiometric target. The latter range also reflects the estimated uncertainty in the site occupancies. Although the data seem quite noisy, the clear difference in step

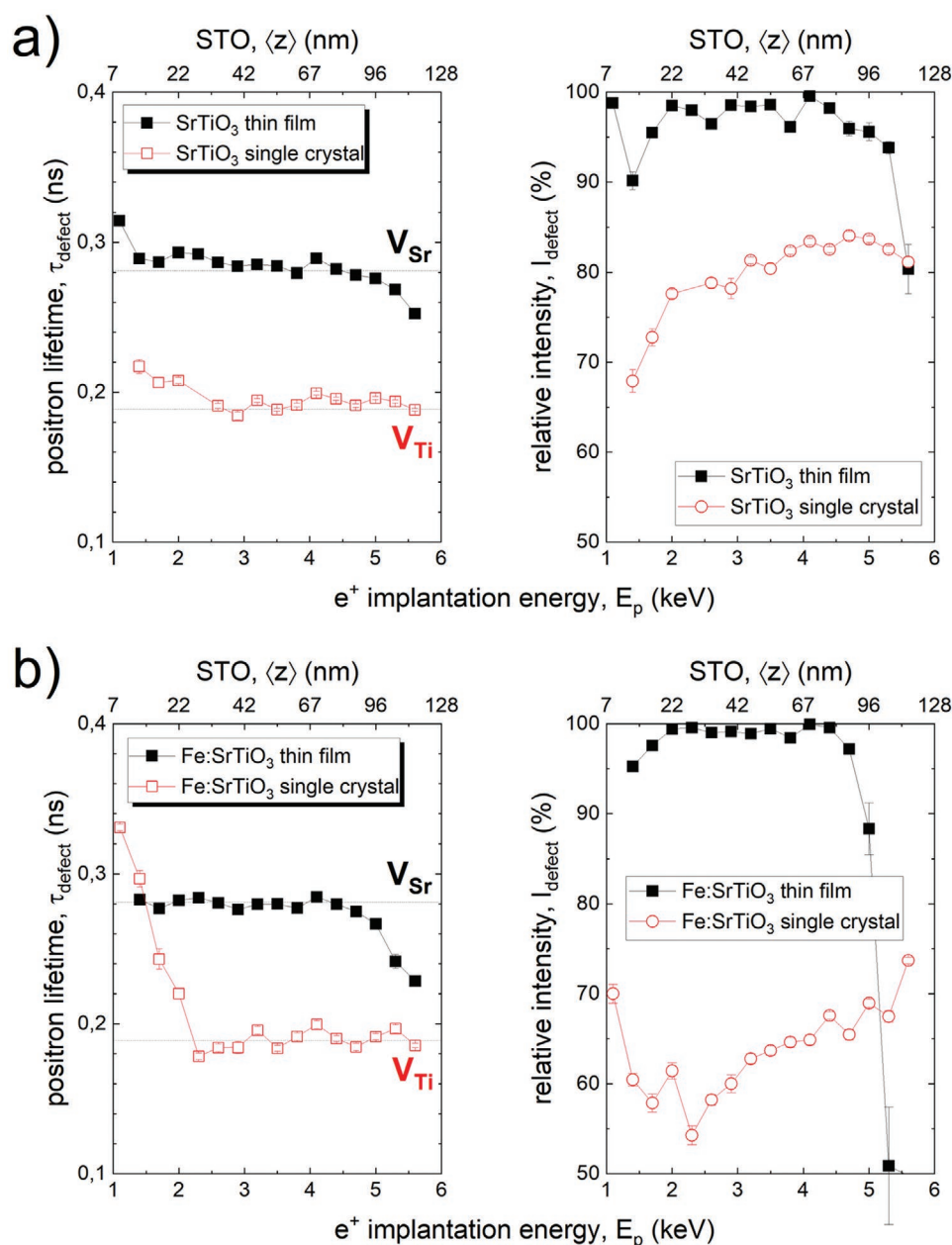


Figure 4. Positron lifetime annihilation spectroscopy (PALIS) measurements to reveal the types of point defects present in thin films and single crystals. a) The most dominant point defects found in a nominally undoped SrTiO₃ thin film are compared to those of a nominally undoped SrTiO₃ single crystal. b) Results for a thin film deposited from a 2% Fe-doped SrTiO₃ target are contrasted with the respective defects found in an Fe-doped single crystal with 0.15% Fe. A significant change in the defects found in thin films and single crystals can be observed for both cases. In thin films, Sr vacancies are the dominant point defect, whereas in single crystals titanium vacancies are identified.

height when crossing the Bragg condition is significant and shows a clear difference between the two samples. Sr deficient films deposited from stoichiometric targets have 30–40% of Fe located at the A-site. On the other hand, in films deposited from a target with 5% Sr excess (i.e., Sr_{1.05}Ti_{0.98}Fe_{0.02}O₃) in order to compensate Sr-loss in the deposition process,^[60] Fe is only present on the B-site. A change in site occupation toward the A-site in SrTiO₃ was also reported for other transition metals, for example, Mn.^[8,81] Such a redistribution of Fe toward the A-site in Sr deficient thin films may have a severe impact on the

defect chemistry, since Fe at the B-site is an acceptor, while Fe at the A-site acts as a (probably deep) donor.

2.6. X-Ray Absorption Spectroscopy

Figure 6a shows X-ray absorption spectra of the Fe L_{2,3}-edge, Ti L_{2,3}-edge, and O K-edge in fluorescence mode for Fe-doped SrTiO₃ thin films deposited from a stoichiometric target with 2% Fe. In order to gain a deeper understanding of the Fe

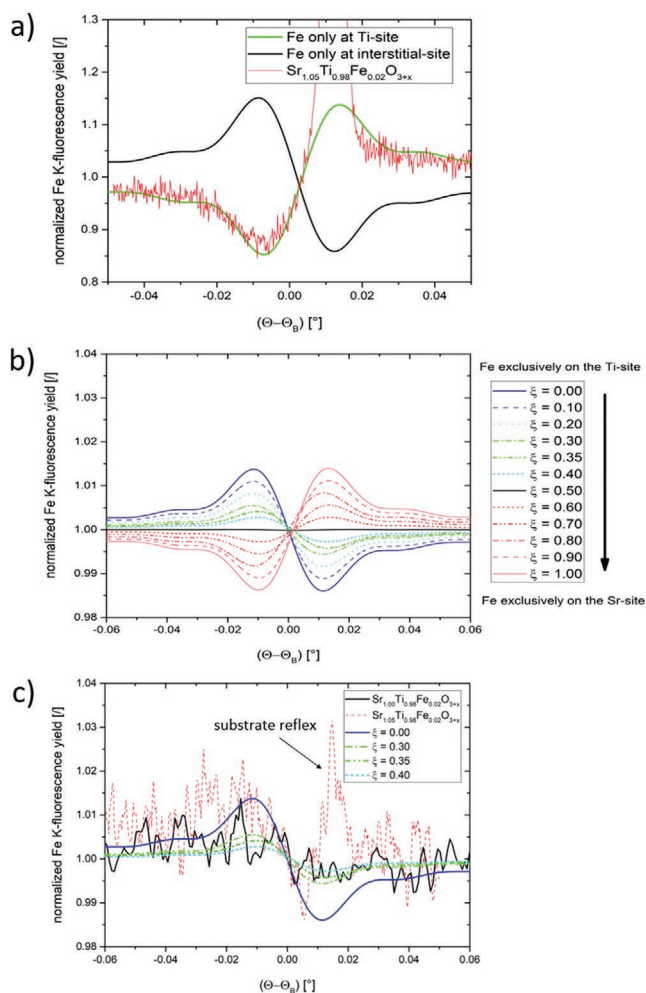


Figure 5. By using X-ray standing wave measurements (XSW), the position of Fe in Fe-doped SrTiO₃ thin films deposited on SrTiO₃ single crystals was determined. Two types of 2% Fe-doped thin films were compared: a thin film deposited from a target with the proper stoichiometric composition (Sr_{1.00}Ti_{0.98}Fe_{0.02}O₃) and a thin film deposited from a target with 5% Sr excess (Sr_{1.05}Ti_{0.98}Fe_{0.02}O₃). According to literature,^[60] the latter leads to a thin film without (severe) cation non-stoichiometry. a) Normalized Fe K-fluorescence yield induced by the interference field of the (002) reflection of Fe-doped SrTiO₃ thin film deposited from a 5% Sr excess target. The measurement indicates that Fe is not present at an interstitial position, but exclusively at the A- and/or B-site. To differentiate between A- and B-site occupancy, b) simulations and c) measurements of the Fe K-fluorescence yield at the (003) reflection are necessary. $\xi = 0$ denotes B-site occupation only, whereas for $\xi = 1$ Fe is present at the A-site only. In the XSW measurements of a thin film deposited from the stoichiometric target (Sr_{1.00}Ti_{0.98}Fe_{0.02}O₃) and a thin film deposited from a target with 5% Sr excess (Sr_{1.05}Ti_{0.98}Fe_{0.02}O₃), differences in the site occupation of Fe can be found. The results suggest that ≈ 30 –40% Fe is present at the A-site in the film deposited from the stoichiometric target. Sr excess in the target seems to prevent A-site occupancy of Fe. (Please note that the influence of the SrTiO₃ substrate reflection is visible in the data of the thin film deposited from the target with 5% Sr excess. The substrate reflection for the thin film deposited from a stoichiometric target occurs at higher angles, that is, the difference between the lattice parameter of the substrate and the thin film is more pronounced for the film deposited from the stoichiometric target.)

oxidation states present in our system, simulations and linear combinations of calculated reference spectra were carried out. Since the simulated Fe⁴⁺ spectra did not fit the experimental data (as also reported in literature),^[57] only Fe²⁺ and Fe³⁺ were considered in the following (see Section S3, Supporting Information). For the simulations, we set the Slater integral reduction to 80% and reduced core spin orbital coupling by 1.0% for Fe³⁺ and 1.1% for Fe²⁺. The valence spin orbital coupling amounted to 3.70% and 3.25% for Fe²⁺ and Fe³⁺, respectively. The crystal field parameters were fixed to 10Dq = 1.5eV and the charge transfer parameters to $\Delta = 2$ eV. Lorentzian broadening was set to 0.2eV and Gaussian broadening to 0.3eV. Based on these parameters, the best agreement between experimental data and the calculated spectra was achieved for 10% Fe²⁺ and 90% Fe³⁺. (Note that these values are only rough estimates due to the fact that self-absorption, site occupation, and oxygen vacancies as well as cation vacancies are not considered here, which might also explain the deviation of the simulated spectra from the measured ones at higher energies).^[57]

When comparing the sample measured directly after the PLD process (0.15mbar O₂ at 700 °C) with the sample with an additional annealing step (200 mbar O₂ at 650 °C), no significant changes can be observed, which means that the thin film ratio of Fe²⁺ to Fe³⁺ is more or less independent of the oxygen partial pressure from 0.15 to 200mbar. In bulk samples, oxygen incorporation is expected under these conditions, corresponding to an increase in Fe oxidation state. However, this deviation from bulk behavior is in good agreement with the oxygen partial pressure independent conductivity measurements presented above (see Figure 2b for a thin film with 0.4% Fe).

The O K-edge and Ti L_{2,3}-edge spectra (see Figure 6b,c, respectively) do not change significantly upon annealing as well and are both in good agreement with literature.^[82–84] The peaks in the O K-edge spectra can be assigned to electron transitions from the O(1s) level into O(2p) orbitals hybridized with Ti(3d) orbitals at 532.2eV and 534.6eV, Sr(4d) orbitals at 537.2eV and 538.9eV, and Sr(5p) orbitals at 544.7eV.^[82] The Ti L_{2,3}-edge spectra show as expected two pre-edge peaks^[85] and a splitting into t_{2g} and e_g levels of the L₃-edge (at 459.0eV and 461.3eV) and the L₂-edge (at 464.4eV and 466.8eV).^[84,85] The results obtained for total electron yield for Fe L_{2,3} are discussed in the Section S4, Supporting Information.

2.7. Conclusions from Thin Film Analysis

Before we begin the discussion of our proposed model we briefly summarize the main conclusions drawn from the different analysis techniques: Our SrTiO₃ thin films grown by pulsed laser deposition from stoichiometric targets show very low DC conductivities, close to those of intrinsic STO, regardless of doping or *p*_o (EIS). They exhibit Sr deficiency of several percent (ICP-OES, RBS). They grow single phased and epitaxially on STO single crystal substrates, and show an elongated *c*-axis (RSM) suggesting Sr-vacancies (confirmed by PALS). Dopand ions (Fe) occupy both the B-site (Fe_{Ti}) and the A-site (Fe_{Sr}) (XSW) in oxidation states of Fe²⁺ and Fe³⁺ (XAS).

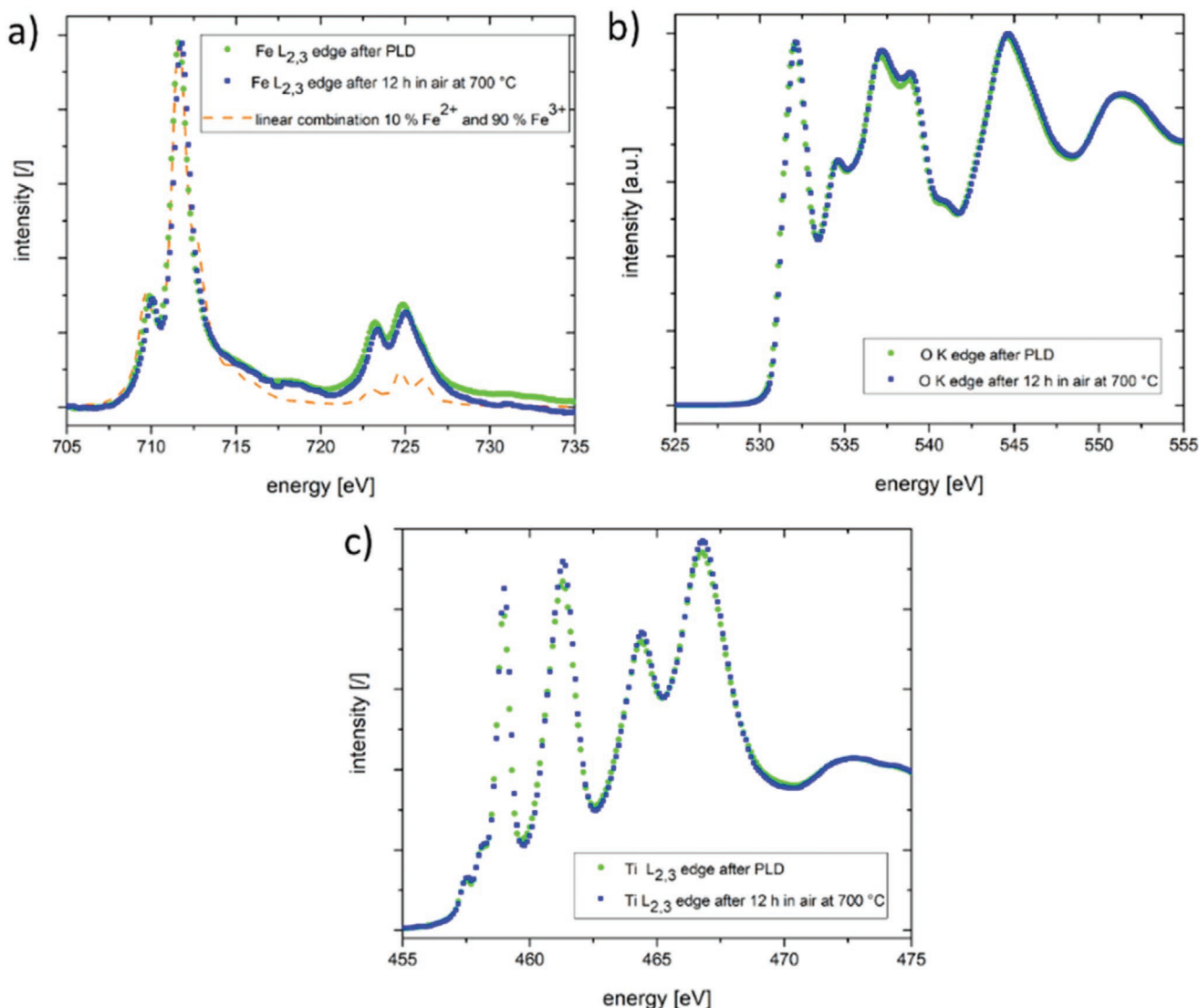


Figure 6. X-ray absorption measurements in fluorescence mode showing the a) Fe L_{2,3}-edge, b) O K-edge, and c) Ti L_{2,3}-edge of Fe-doped SrTiO₃ thin films deposited from a stoichiometric target with 2% Fe directly after the pulsed laser deposition (green dots) and after an additional annealing step at 700 °C in air for 12 h (blue squares). A linear combination of 10% Fe²⁺ and 90% Fe³⁺ (orange dashed line) matches the experimental data best.

3. Discussion

3.1. Basic Model

Based on all the experimental results a model is now introduced and discussed, explaining the “ubiquitous” pseudo-intrinsic behavior of SrTiO₃ thin films. The extraordinary effect occurs for Fe-doped SrTiO₃ with Fe contents from 0.4 to 10%, for Ni-doped SrTiO₃ and Al-doped SrTiO₃, and even for undoped SrTiO₃. Also, p_{O_2} variations do not change conductivities between 10⁻⁵ and 1 bar. Essentially, we have to explain why the Fermi level seems to be pinned close to mid-gap in all these cases.

We start the model discussion with the truly intrinsic case, that is, with the Fermi level being exactly mid-gap and negligible oxygen vacancy concentration, see **Figure 7a**. Such a situation would require ultra pure SrTiO₃ films with impu-

urity levels in the sub ppb range since, for example, at 420 °C [h^+] = [e^-] values are as low as 10¹¹ cm⁻³. Such a purification of the films during deposition is completely unrealistic and also contradicts the chemical analysis. Adding an acceptor dopant shifts the Fermi level toward the valence band (**Figure 7b**). The acceptor dopants used in this study (Fe, Ni, Al) are known to act as deep traps for holes and thus the Fermi level is below the acceptor level and quite far from mid-gap. (Please note: In this first consideration we neglect the oxygen vacancies formed by acceptor doping of SrTiO₃, this is further discussed below). Adding a donor dopant to the system shifts the Fermi level upward, but only for a very specific donor concentration the acceptors are exactly counter-balanced, and a mid-gap situation is met, **Figure 7c**. This case can also be excluded here due to the ubiquity of the effect.

Combining additional acceptor-type mid-gap states (acceptor 2) and the main acceptor 1 doping does also not explain the

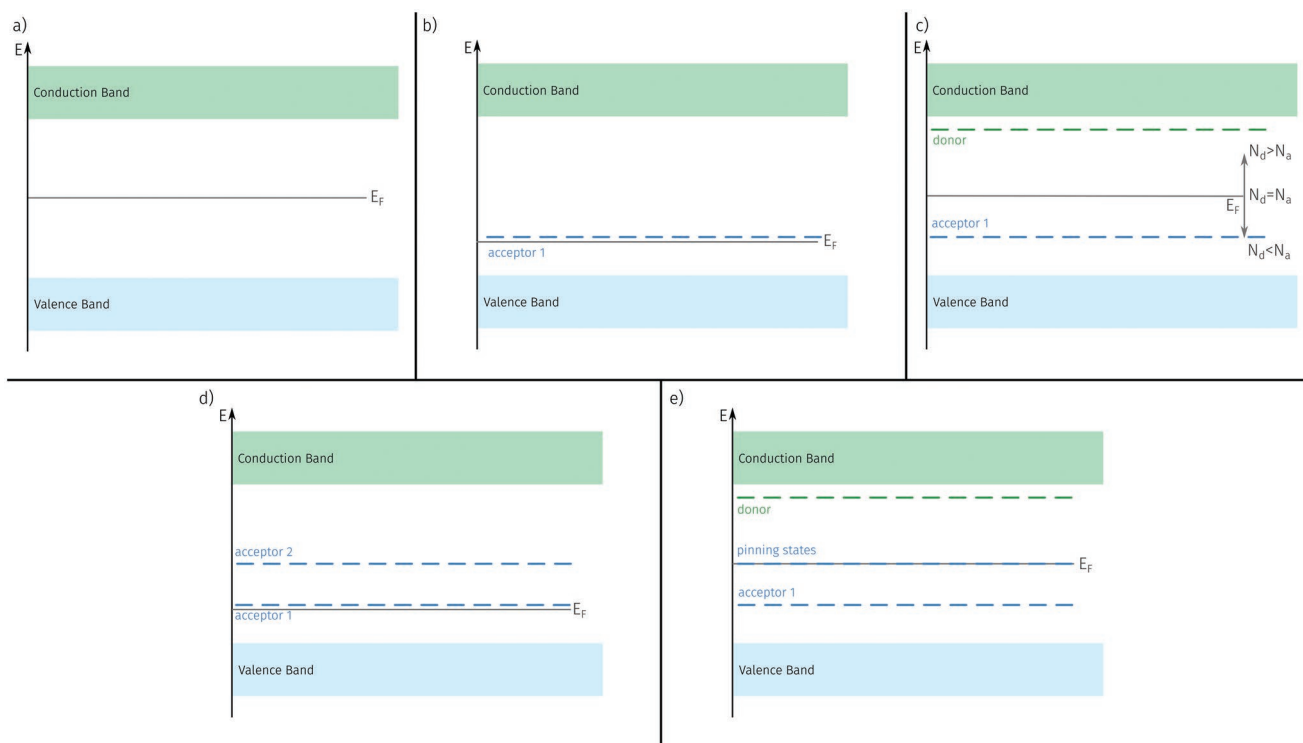


Figure 7. Band structure of SrTiO₃ for different doping cases. a) Fermi level is mid-gap, corresponding to intrinsic concentrations in a semiconductor. This is the hypothetical case of ultra pure, defect-free, stoichiometric SrTiO₃. b) With the introduction of acceptor states (acceptor 1), the Fermi energy is adjusted accordingly. Here a deep acceptor is shown, with both acceptor and donor dopants present. c) For exactly equal amounts of acceptor and donor states, the Fermi level is mid-gap. When the acceptor/donor ratio differs from unity, the Fermi level moves to the more dominant state. Hence, the Fermi level is not pinned at mid-gap in a robust manner. d) If instead of the donor in (c) a mid-gap acceptor (acceptor 2) is added, the Fermi level is mostly dominated by the acceptor 1 states. e) Both acceptor (acceptor 1), donor, and mid-gap states (acceptor 2) are present, allowing robust mid-gap Fermi level pinning.

situation. This would leave the Fermi level far from mid-gap (Figure 7d). However, a rather robust mid-gap situation results when combining acceptors 1, mid-gap acceptors 2 and donors (Figure 7e). For a reasonably broad range of doping concentration ratios, this indeed pins the Fermi level close to mid-gap, as illustrated in detail below. More specific, acceptor 1 is not even required, since already mid-gap acceptor states and a donor are sufficient to cause a Fermi level pinning. A similar three level model was also discussed for semi-insulating GaAs with Cr impurities.^[86]

This model has a simple chemical analogy. Ultra-pure water exhibits a pH value of 7. Adding a (weak) acid lowers the pH value (corresponding to our acceptors causing positive holes). When adding NaOH solution the pH raises and for a very specific amount of NaOH the pH of the aqueous solution might be 7 (see also below). However, the slightest deviation from this specific amount either leads to acidic or alkaline solutions, respectively. When adding another acid with a pK_S value of seven to the first acid (instead of adding NaOH), the pH value becomes even slightly lower than before. However, for a solution with weak acid 1 (= acceptor doping in our case) and weak acid 2 (with $pK_S = 7$, corresponding to the acceptor with mid-gap states here), we can “activate” the $pK_S = 7$ buffer system with a proper amount of NaOH. (The proper amount is approximately the amount of acid 1 plus half of the amount of acid 2). Accordingly, the pH-value is pinned at around $pH = 7$. This

analogy is further discussed in Section S6, Supporting Information. Please note that such a buffer also works without acid 1.

With this electronic “buffer system” we now have a basic model for explaining the pseudo-intrinsic behavior of SrTiO₃. In a next step we have to specify the required acceptor and donor states. The identity of acceptor 1 in the doped SrTiO₃ samples is obvious, it is either Fe, Ni, or Al. In undoped SrTiO₃ it is irrelevant, since the mid-gap pinning does not require such acceptor 1 dopants anyway, provided mid-gap acceptor states and additional donors are present. In the following, we discuss what may lead to the two essential states in our pseudo-intrinsic SrTiO₃ thin films, the acceptor-type mid-gap states and the donor states.

3.2. Specific States Relevant in the SrTiO₃ Films

First, mid-gap states are considered. Compositional (ICP-OES, RBS), structural (RSM) as well as defect analysis (PALS) point toward Sr (or A-site) vacancies being present in all doped and undoped SrTiO₃ thin films. Such Sr vacancies act as acceptors in SrTiO₃ and lead to electron holes. (Partial counterbalancing by oxygen vacancies is neglected at this stage, see below). We assume that the energy of the first hole trapping

$$V'_{Sr} \rightleftharpoons V''_{Sr} + h^{\bullet} \quad (1)$$

is mid-gap, while the second hole trap

$$V_{Sr}^{\times} \rightleftharpoons V_{Sr}' + h^{\bullet} \quad (2)$$

is shallow.^[87] Interestingly, such a mid-gap energy of Sr vacancies was already suggested in ref. [2], where it was assumed without experimental evidence. The reaction in Equation (2) simply adds further holes to those created by other acceptors dopants such as Fe. The formation of V_{Sr}' by a hole trapping of V_{Sr}'' (Equation (1)), however, can pin the Fermi level in the mid-gap range. Please note, that the supposed mid-gap energy of the Sr vacancy is specific for SrTiO₃ and can be expected to be different in other perovskite-type oxides, also titanates. Moreover, it is not necessarily exactly mid-gap since also reduced electron and hole mobilities in defect-rich thin films may play a certain role for the observed pseudo-intrinsic behavior. For example a deviation of the pinned state from mid-gap by plus or minus 30 meV together with a factor 3 lower mobility would again lead to pseudo-intrinsic conductivities.

Second, possible donor states have to be considered. As mentioned before, partial occupation of the A-site by typical B-site cations is a realistic option. In literature, a redistribution of Mn to A-sites was experimentally found^[8,81,88–90] and changes in the site occupation were also suggested for Cr,^[10] Er,^[11] and Rh.^[13,14] Moreover, such changes in site occupation are discussed in other perovskite type titanates, for example, Mg,^[91] Eu,^[91,92] or Y^[93] in BaTiO₃, Mn^[94] in CaTiO₃, and Al^[95] in (Na,Bi)TiO₃. Also our XSW measurements reported above indicated significant amounts of Fe on the A-site. Such a site change of Fe leads to a change of its dopant character, with Fe at the A-site being a donor dopant according to



Owing to the larger ionic radius of Fe²⁺ (Fe_{Sr}^{\times}) compared to Fe³⁺, that is, a better fit of Fe²⁺ to the A-site, the corresponding trapping energy of Equation (3) might be quite high and the corresponding energy level can be expected to be far below the conduction band. However, as long as the corresponding level is above mid-gap, this site change would not only reduce the concentration of energetically unfavorable Sr vacancies but would also introduce donor states to activate the mid-gap Fermi level pinning.

The XSW measurements (see Figure 5) and XAS measurements (see Figure 6) might give a first clue to the energy position of the A-site Fe donor states. From the XAS study we can estimate about 10% Fe²⁺ and 90% Fe³⁺, after annealing in air. The XSW measurements indicate that about one third of Fe is at the A-site. All Fe²⁺ is attributed to the A-site, the rest of the Fe at the A-site is thus in the Fe³⁺ state, resulting in a mixture of one third Fe²⁺ and two thirds Fe³⁺ at the A-site. This mixture in oxidation state tells us that the corresponding Fe donor states at the A-site are just slightly above the Fermi level (which must be close to mid-gap according to conductivity measurements), see **Figure 8**. This estimate is certainly prone to some errors and also a Fe_{Sr}^{\times} level beneath mid-gap is conceivable. However, the existence of Fe²⁺ despite mid-gap Fermi level pinning excludes that the Fe_{Sr}^{\times} level is far above

mid-gap and thus Fe is probably not the donor state we are looking for in our model. Moreover, Fe_{Sr}^{\times} could not explain pseudo-intrinsic behavior for other acceptor dopants (Ni, Al) and undoped SrTiO₃.

Hence, we suggest Ti on A-sites as the decisive donor present in all the different films. Those were observed experimentally and predicted theoretically in literature^[15–17,96] and can act as a donor according to



which is supposed to be far above mid-gap, perhaps even close to the conduction band. This is also sketched in Figure 8. Therefore, already the existence of A-site vacancies and Ti ions on A-sites can explain the pseudo-intrinsic behavior. Additional dopants such as Fe then add further states, depending on their site, but do not change the essential effect, that is, Fermi level pinning very close to mid-gap.

So far, oxygen vacancies as donors were neglected, even though it is known that their concentration can be substantial in acceptor doped SrTiO₃.^[97,98] However, SrTiO₃ bulk defect chemistry models^[1] suggest that for electronically intrinsic thin films (i.e., low $[h^{\bullet}]$), the oxygen vacancy concentration $[V_{O}^{\bullet}]$ is also very low due to the mass action law

$$K_{\delta} = [h^{\bullet}]^2 [V_{O}^{\bullet}]^{-1} p_{O_2}^{-0.5} \quad (5)$$

of the oxygen incorporation reaction



At 600 °C, for example, we have at the intrinsic point $[h^{\bullet}] = 2.7 \times 10^{13} \text{ cm}^{-3}$ and for $p_{O_2} = 1$ bar this leads to $[V_{O}^{\bullet}] = 5.8 \times 10^{10} \text{ cm}^{-3}$. Hence, neglecting free oxygen vacancies in our model seems to be justified. Indeed, ionic conductivities are very low in low Fe-doped SrTiO₃ thin films.^[60] However, it increases for higher doping concentrations and the reasons behind this dopant dependence of the ionic conductivity in otherwise electronically pseudo-intrinsic films are not known yet.

Defect associates are a possible explanation and they further modify the picture sketched above. With Sr vacancy concentrations in the percentage range, defect interaction between negatively charged Sr vacancies and positively charged oxygen vacancies are not only possible, but rather likely.^[19,20] Also, dopant-vacancy interaction can be expected.^[99,100] Such a defect interaction may increase the total oxygen vacancy concentration compared to that of Equation (5). However, the general model suggested here for explaining the pseudo-intrinsic behavior (acceptor-type mid-gap species due to Sr vacancies and Ti-cations on A-sites as donors) is not affected by these complications.

Actually, our model explaining pseudo-intrinsic behavior does not require a specific donor (e.g., Ti on A-sites) and thus also nominally donor doped SrTiO₃ thin films with A-site deficiency might exhibit such a behavior. Indeed, preliminary measurements on such films (deposited from targets with 0.4% Nb doping) lead to very low conductivities, see Section S5, Supporting Information, even though still somewhat higher than the pseudo-intrinsic conductivity. Possibly, the added donor (Nb) drives the Sr vacancy buffer states to almost complete

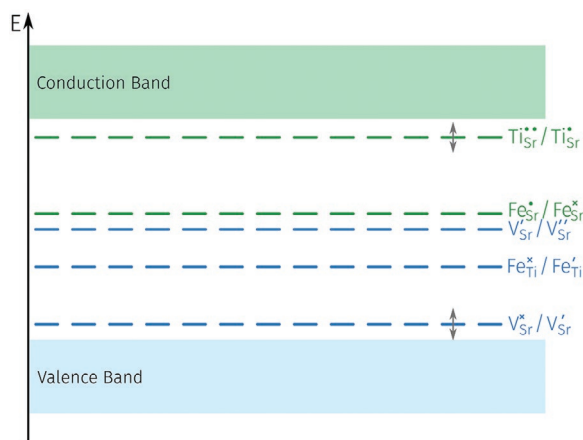


Figure 8. Suggested band structure of our pseudo-intrinsic Fe-doped SrTiO₃ thin films. Fe at the B-site (Fe_{Ti}^{••}/Fe_{Ti}^{••}) works as an acceptor. We suggest V_{Sr}^{••}/V_{Sr}^{••} states in the middle of the band gap. Site changes caused by Sr vacancies lead to donor states. Most important is Ti on the A-site, Ti_{Sr}^{••}/Ti_{Sr}^{••}, corresponding to shallow donor states. The levels corresponding to Fe_{Sr} defects are deep donors, slightly above mid-gap. Sr vacancies also act as acceptor states close to the conduction band (V_{Sr}^{••}/V_{Sr}^{••}). Arrows indicate that the position of several states in the band-gap is a first estimate; our model does not depend on their exact position (within a certain range).

V_{Sr}^{••} and thus the Fermi level begins to leave the pinned mid-gap position.

This model is also in accordance with the experimental fact that bulk-like conductivity can be reached in SrTiO₃ thin films when using PLD targets with a rather pronounced Sr overstoichiometry of about 7%.^[60] Such thin films are stoichiometric and show V_{Ti}V_O clusters in PALS studies as predominant point defects, while Sr vacancies are no longer seen. Thus, the Fermi energy is then defined by the common Fe_{Ti} acceptor level and indeed the hole conductivity expected from macroscopic Fe-doped samples is obtained in such films.

Moreover, we expect a similar effect also in thin films of other large band gap materials which are prone to cation nonstoichiometry due to the preparation process, for example, PLD. The resulting cation vacancies may trigger some site changes and thus states that can cause Fermi level pinning. However, the pinned position of the Fermi level is not necessarily very close to mid-gap. Thus, a doping insensitive conductivity may result for many other materials, but the value might be different from the pseudo-intrinsic case found for SrTiO₃. (The chemical analogue are again buffer systems. Most of them buffer at pH values different from 7).

3.3. Model Calculations for Testing the Consistency of the Model

So far, we discussed that in a system consisting of donor states (Ti_{Sr}^{••}/Ti_{Sr}^{••} in our case) and buffering mid-gap acceptor states (V_{Sr}^{••}/V_{Sr}^{••} in our case) the Fermi level can be pinned close to the intrinsic point, that is, mid-gap. Still, it is somewhat surprising that the corresponding pseudo-intrinsic behavior is found for so many different dopants and doping levels as well as oxygen

partial pressures. In the following estimates and calculations, we discuss the sensitivity of this pinning situation to changes in the acceptor/donor ratio and show why the pseudo-intrinsic situation is so often met. More specific, we illustrate why neither the exact Sr/Ti ratio, nor the dopant ion and its exact concentration seems to be very critical for obtaining the effect.

We start with some general estimations about this electronic buffer system. First, the concentration of mid-gap buffer (i.e., Sr vacancies) needs to be higher than that of other dopants with possibly varying ionization, for example, higher than that of Fe acceptor doping on the B-site. Thus, up to a few percent of Sr vacancies are required, at least in the highly Fe-doped films. Such a high amount of Sr vacancies is well in line with our experimental data found for such thin films, see Table 1. Moreover, Fe on the A-site reduces the amount of acceptor-type Fe and thus of required Sr vacancies. As a second prerequisite, the amount of acceptor and donor doping must be in the same concentration range. More specific, an ideal buffer situation is met if 50% Sr vacancies trap one hole (V_{Sr}^{••}) and 50% trap no hole (V_{Sr}^{••}), while all other acceptors (here Fe on the B-site) are filled by holes. The ideal singly charged donor concentration is thus 1.5 times the amount of Sr vacancies plus the amount of Fe dopant on the B-site. Accordingly, we have ideally 0.75 (doubly charged) Ti_{Sr}^{••} per Sr vacancy in undoped SrTiO₃.

Any deviation from such an ideal ratio between acceptor and donor dopant is then balanced by a shift of the Sr vacancy ionization between V_{Sr}^{••} and V_{Sr}^{••} and thus the electron and hole concentrations remain close to the intrinsic level (like the pH in a chemical buffer with pK_S = 7). Indeed, in PALS measurements a decreased positron lifetime indicates a change in the V_{Sr} ionization after annealing in air without changing the film conductivity. As a consequence, it is not required to have exactly fitting concentrations of donor states (e.g., Ti on A-site) or Sr vacancies for reaching the Fermi level pinning.

We can further quantify this model for exemplary cases, in order to see whether our assumptions truly explain the “ubiquity” of the pseudo-intrinsic behavior in SrTiO₃ films despite changes of acceptor/donor ratios and oxygen partial pressure. In a first step we consider nominally undoped SrTiO₃. From the hole trapping equilibria of Sr vacancies (Equations (1) and (2)), the band-band equilibrium of electrons and holes

$$\text{nil} \rightleftharpoons e' + h^{\bullet} \quad (7)$$

the trapping reaction of Ti_{Sr} (Equation (4)) and the oxygen exchange reaction in Equation (6), we can numerically calculate all defect concentrations for a given Sr/Ti ratio. In Figure 9 this is done for the experimentally found Sr/Ti ratio of 0.918; defect equilibrium values of Equation (6) are taken from ref. [2] and the electronic energy levels and equilibrium constants are listed in Table 2. This set of parameters is also used in all other subsequent calculations. Figure 9a displays how the defect concentrations, and particularly the electron and hole concentrations, depend on the A-site fraction of Ti. A Ti fraction of 2.5% on the A-site corresponds to the ideally buffered case (75% of the total V_{Sr} concentration). Between ≈2.2% and 2.7% Ti_{Sr} donors, the sum of the electron and hole concentration varies only by a factor of two and thus a very similar (pseudo-intrinsic)

Table 2. Energy levels of electronic states in Fe-doped SrTiO₃ at 400 °C used for calculating defect concentrations and testing the consistency of our model. Energy levels are given in units of the band gap energy E_g relative to the valence band edge ($E_g = 3.3$ eV), and equilibrium constants K_i are given in defects per unit cells (UC). The exact values of the guessed energy levels do not affect the outcome of the calculation as long as they are comparatively close to the band edges.

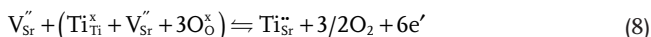
Reaction	Mass action law	Energy level	K_i (/UC)	Value from
$V_{Sr}'' \rightleftharpoons V_{Sr}' + h^*$	$K_1 = [V_{Sr}'] [h^*] [V_{Sr}'']^{-1}$	$E_g \times 0.500$	2.4×10^{-12}	This study
$V_{Sr}^x \rightleftharpoons V_{Sr}' + h^*$	$K_2 = [V_{Sr}'] [h^*] [V_{Sr}^x]^{-1}$	$E_g \times 0.1$	4.7×10^{-3}	Our estimate
$Fe_{Sr}^x \rightleftharpoons Fe_{Sr}' + e'$	$K_3 = [Fe_{Sr}'] [e'] [Fe_{Sr}^x]^{-1}$	$E_g \times 0.513$	4.7×10^{-12}	This study
$Ti_{Sr}^x \rightleftharpoons Ti_{Sr}' + e'$	$K_4 = [Ti_{Sr}'] [e'] [Ti_{Sr}^x]^{-1}$	$E_g \times 0.9$	4.7×10^{-3}	This study
$Fe_{Ti}^x \rightleftharpoons Fe_{Ti}' + h^*$	$K_5 = [Fe_{Ti}'] [h^*] [Fe_{Ti}^x]^{-1}$	$E_g \times 0.333$	1.76×10^{-8}	Ref. [1]

conductivity results in this range, see Figure 9b. Accordingly, we do not need an extremely precise balancing of acceptors (V_{Sr}) and donors (Ti_{Sr}) on the level of ppb, though a reasonably good match of the Ti_{Sr} concentration is required for explaining pseudo-intrinsic behavior, see discussion below.

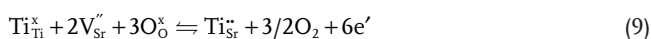
The pronounced insensitivity of the electron and hole concentration to p_{O_2} variations in the range of 10^{-5} to 1 bar is clearly confirmed by the calculations. In Figure 9c the resulting Brouwer diagram is shown for a perfectly matching acceptor to donor ratio of our undoped SrTiO₃ thin film, that is, for (Sr_{0.94}Ti_{0.025}V_{0.035})TiO_{3- δ} . The electron and hole concentrations are very close to the intrinsic value over a wide oxygen partial pressure range. We get the same results also for many other donor to acceptor ratios. Moreover, a very similar situation is found for the Fe-doped samples: excellent insensitivity to p_{O_2} , but only mediocre insensitivity to the amount of Ti on A-sites. The corresponding results for Fe-doped films are shown in Section S7, Supporting Information.

3.4. Self-Limitation of the Ti Site Change Reaction

This leaves us with the question why the amount of Ti on A-sites fits to the donor/acceptor range needed for explaining the very robust pseudo-intrinsic situation, that is, why we get an Ti_A fraction of 2.2–2.7% in the case discussed above, and why this works for different Sr/Ti ratios, different dopants and different doping levels. At first sight one might think that annihilation of a Sr vacancy by a site change of Ti is either energetically favorable, and thus takes place to a large extent, or is unfavorable and hardly occurs at all. However, the corresponding reaction for a Sr/Ti ratio smaller than unity is more complex. It reads



or



The site change of one Ti ion leads to the annihilation of one perovskite unit cell ABO₃ (indicated by the brackets in Equation (8)) and thus reduces the number of Sr vacancies by two. Notably, this reaction is different from an antisite defect formation



Due to the high formation enthalpies of Sr_{Ti}'' and Ti_{Sr}'' this reaction is often considered energetically unfavorable and thus neglected.^[101] In contrast, in our site change reaction there is only one very unfavorable defect produced (Ti_{Sr}'') but its formation is counteracted by the annihilation of two also unfavorable Sr vacancies. It is therefore very reasonable to assume that the site switch reaction (Equation (9)) is energetically more favorable than the antisite defect formation (Equation (10)).

Please note that exact cation stoichiometry of PLD grown thin films is often governed by growth kinetics rather than bulk thermodynamics. Despite this, we may attempt a thermodynamic treatment given the following considerations: of the defect chemical reactions included in our calculations, most are electronic excitations between either conduction or valence band or band gap states, specifically Equations (1), (2), (4) and (7). These are probably sufficiently fast to equilibrate on timescales much shorter than the film growth. The oxygen exchange reaction, Equation (6), is likely also fast at the deposition temperature of 600 °C. This leaves the site-change reaction, Equation (9). Here we assume that in the topmost, currently growing layer the ion mobility, due to low coordination number, is sufficiently high to allow the layer to reach a (potentially metastable) equilibrium. In the buried bulk layers below, however, this state is then likely frozen-in, due to the low cation vacancy mobility in SrTiO₃.^[2,102] Possibly, the site-change reaction may not reach its equilibrium state exactly, that is, the Ti_{Sr} concentration may be slightly different from its equilibrium value, also because surface equilibrium may differ from bulk equilibrium. Below we demonstrate that a pseudo-intrinsic conductivity still occurs as long as the Sr_{Ti} concentration does not deviate from its equilibrium value too far.

Interestingly, the site change reaction also leads to electrons on the product side, and thus a high concentration of electrons is detrimental for the reaction. Let us now assume a reaction enthalpy and entropy such that the site change reaction is still favorable for a mid-gap Fermi level. Many site changes might then lead to such a large number of electrons that essentially all Sr vacancies become V_{Sr}'' and thus the electronic mid-gap buffer system is over-crowded. The Fermi level moves toward the conduction band, the Gibbs free energy of the product side in Equation (9) becomes unfavorable and the Ti_{Sr} formation is stopped. This kind of self-limitation is responsible for the Ti_{Sr}

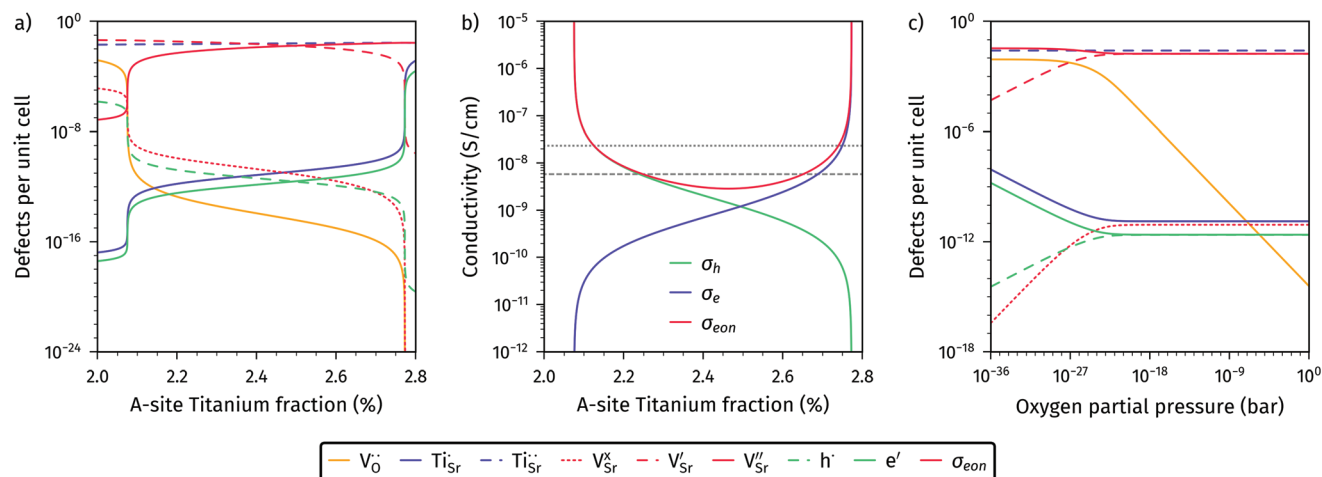


Figure 9. Defect chemical calculations at 400 °C for the defect chemical parameters in Table 2 and Ref. [1]. (a) Defect concentration against A-site Ti fraction, constrained to the elemental composition determined by ICP-OES, i.e. Sr/Ti = 0.918 and p_{O_2} of 1 bar. (b) Corresponding electron, hole and sum conductivities. (c) A Brouwer diagram for Sr deficient undoped SrTiO₃ with Ti partly on the A site (Sr_{0.941}Ti_{0.025})TiO_{3-δ}.

fraction not exceeding a level that keeps the Sr vacancy buffer still active. In other words, this self-limitation automatically establishes the proper acceptor/donor ratio. Therefore, mid-gap pinning of the Fermi level results in many cases.

The same argumentation can also be expressed in terms of the corresponding mass action law:

$$K_{Ti_{Sr}} = p_{O_2}^{3/2} \frac{[Ti_{Sr}^{2+}][e']^6}{[V_{Sr}^{2+}]^2} \quad (11)$$

A mid-gap Fermi level requires substantial concentrations of Ti_{Sr} as well as V_{Sr} and thus $[V_{Sr}^{2+}] \gg [e']$ and $[Ti_{Sr}^{2+}] \gg [e']$. Due to charge neutrality, any substantial change of the donor concentration, that is, of $[Ti_{Sr}^{2+}]$, would require very strong relative changes of the small $[e']$, which is not compatible with Equation (11). Hence, further formation of Ti_{Sr} does not take place and the Fermi level stays pinned. Please note: Even if the (effective) oxygen partial pressure during deposition was different, for example, due to influence of the plasma,^[103] the general model still holds. A different p_{O_2} would mainly change the $K_{Ti_{Sr}}$ window where the buffer effect occurs.

This can be quantified by numerically calculating the Gibbs free energy G of the system for different stages of the site change reaction Equation (9), that is, in dependence of the fraction of A-sites occupied by Ti (Ti_{Sr} per unit cell). **Figure 10a** displays the resulting curves for a specific Sr/Ti ratio (0.918, see experiments), 650 °C, $p_{O_2} = 0.15$ mbar (PLD conditions) and different standard Gibbs free energies ΔG^0 of this reaction. Indeed, a minimum and thus a thermodynamically stable situation results close to the optimal Ti_{Sr} site fraction (between 2.2% and 2.7%), at least for a certain ΔG^0 range. The equilibrium Ti_{Sr} fractions are plotted in Figure 10b for different ΔG^0 , together with the two concentrations of the Sr vacancy buffer system (V_{Sr}^x , V_{Sr}^y). It becomes obvious that for a reasonably broad range of ΔG^0 (between 9.5 and 10.5 eV) the self-limitation of the Ti-site change results in films with acceptor and donor concentrations being such that the Fermi level is pinned close to mid-gap. A comparison of our ΔG^0 with STO defect formation enthalpies

from literature confirms that the suggested energy range is indeed a reasonable estimate.^[101,104,105] This is discussed in detail in the Section S9, Supporting Information.

The robustness of our pseudo-intrinsic conductivity can now be tested by numerically calculating the resulting electronic conductivity for different Sr/Ti ratios and varying ΔG^0 values as well as varying positions of the Sr vacancy level (around mid-gap). In a first step, the equilibrium Ti_{Sr} concentration is determined for given defect parameters and 650 °C, $p_{O_2} = 0.15$ mbar (PLD conditions). Then the resulting Ti_{Sr} fraction is taken as frozen-in and the other defect concentrations are recalculated for 400 °C, $p_{O_2} = 1$ bar. The results are plotted in **Figure 11a–d** with the inner dashed lines indicating the region (bright blue) in which the conductivity is at most twice the intrinsic conductivity. We consistently find pseudo-intrinsic conductivity values despite varying Sr/Ti-ratios as long as ΔG^0 is in the range of ≈ 9.25 –10.5 eV and Sr vacancies are around mid-gap. Not surprisingly, the pseudo-intrinsic behavior does not simply vanish when during pulsed laser deposition the laser energy is varied, leading to a varying Sr/Ti ratio.^[60]

Still these diagrams are a bit misleading. They seem to suggest that also Sr vacancy levels far from mid-gap may cause pseudo-intrinsic conductivities for appropriate ΔG^0 values. This, however, describes just the situation where donors exactly counter balance acceptors in absence of a buffer system. This is visualized in Figure 11e–h, where the conductivity and thus also the pseudo-intrinsic range is plotted versus Sr vacancy level in the band gap and the A-site Ti fraction. Clearly, a significant deviation of the V_{Sr} buffer system from mid-gap strongly reduces the tolerance of the system with respect to exactly established site changes, that is, the concentration of Ti_{Sr}. Essentially, for a nonbuffered pseudo-intrinsic situation the slightest deviation of Ti_{Sr} from its equilibrium value causes large changes of $[e']$ and drastic changes of the r.h.s. in Equation (11). (Hence, a variation of Ti_{Sr} formally corresponds to very strong ΔG^0 change, if the buffered range is left.) Accordingly, a very robust pseudo-intrinsic effect requires V_{Sr} states being approximately mid-gap.

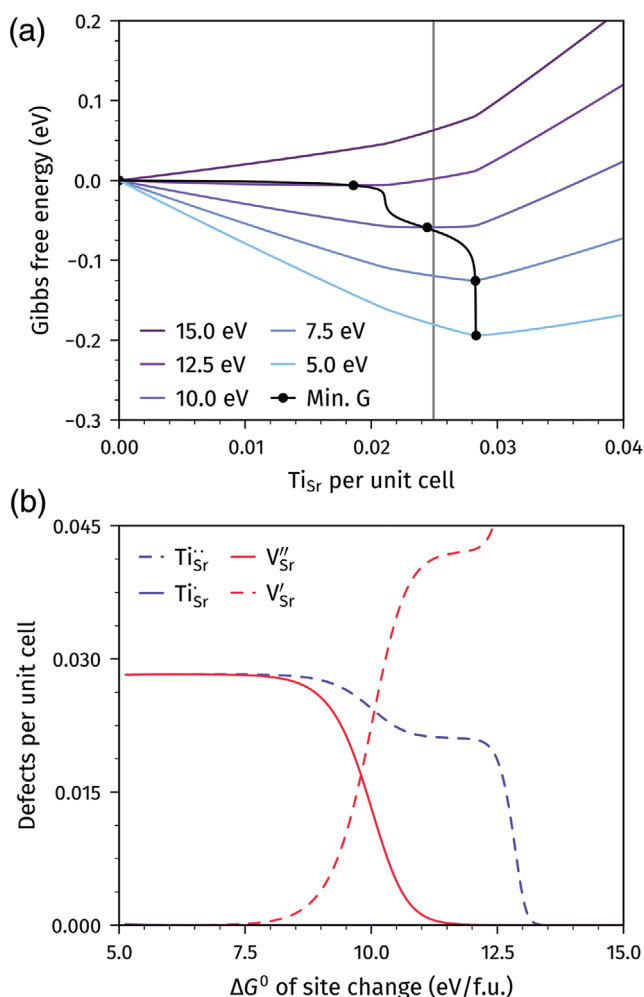


Figure 10. (a) Gibbs free energy G of an undoped $SrTiO_3$ film with $Sr/Ti = 0.918$ calculated for a progressing site change reaction, Equation 8, at $650\text{ }^\circ\text{C}$ and 0.15mbar oxygen partial pressure and different standard Gibbs energies of the reaction ΔG^0 . In a certain range, the minima of G correspond to Ti_{Sr} values with pseudo-intrinsic conductivities. (b) Dependence of several equilibrium donor and acceptor defect concentrations on the standard Gibbs free energy of the site change reaction.

The same stability results when performing such calculations for Fe-doped thin films with a fixed $Sr/(Ti+Fe)$ ratio but varying Fe dopant concentration, see **Figure 12** for the case of $Sr/(Ti+Fe) = 0.90$, Sr vacancies being exactly mid-gap and no Fe on the A site. Hole trapping at Fe_{Ti} is taken into account, but virtually all trap states are filled anyway due to the mid-gap pinning of the Fermi level. Thus, also other acceptor dopants (e.g., Ni, Al) would lead to the same effect as long as their hole trapping level is significantly below mid-gap. We see that up to almost 10% Fe doping for ΔG^0 of the Ti site change reaction between $9.5\text{--}10.5\text{ eV}$ all Fe-concentrations lead to pseudo-intrinsic conductivities (within a factor of two of the exact intrinsic value). A more detailed analysis of this situation is given in the Section S8, Supporting Information, where more $Sr/(Ti+Fe)$ ratios and also Fe on Sr sites are taken into account. Accordingly, the last point of our consistency check is also fulfilled and we dare to say that we truly have a very reasonable model that can explain

the “ubiquitous” low conductivity of $SrTiO_3$ thin films. Accordingly, situations may often result with conductivities pinned to a certain (not necessary ultra low) value and hardly depending on doping or oxygen partial pressure. This effect may either impede an intended tuning of the conductivity by doping, or, in the fortunate case that the vacancy buffer level coincides with a desired conductivity, protect against conductivity changes due to impurities. Owing to the self-regulation of the site changes, we suppose that very similar phenomena also exist in many thin films of other ternary oxides with large band gaps.

4. Conclusion

Ultra low and almost intrinsic electronic conductivity ($[e'] \approx [h^{\bullet}]$) was found for differently doped (Fe, Ni, Al) $SrTiO_3$ thin films, in a broad range of dopant concentrations, and for nominally undoped $SrTiO_3$ thin films. Thin film characterization revealed a substantial Sr vacancy concentration. Fe-doped $SrTiO_3$ thin films were further investigated by XAS and XSW, unraveling a redistribution of Fe toward the A-site of the perovskite. Based on these observations we developed a model explaining the almost ubiquitous pseudo-intrinsic conductivity found in many $SrTiO_3$ thin films. Essential are Sr vacancies as acceptor-type mid-gap states and a donor dopant, which together pin the Fermi level in the middle of the gap. This is analogous to an aqueous system when adding a base to a weak acid of $pK_S = 7$, thus activating the corresponding buffer system and fixing the pH close to 7. Possible donor dopants present in our thin films are discussed and the main source of donors is believed to be B-site ions on A-sites, particularly Ti ions on A-sites. The Ti site change reaction also involves electronic charge carriers and becomes energetically unfavorable when leaving the mid-gap situation. Hence, a kind of self-regulation takes place, leading to the proper amounts of donors (Ti_{Sr}) and acceptors (V_{Sr}) in such a thin film. Accordingly, this effect of a dopant-independent very low conductivity may not only occur under very specific conditions but might be rather ubiquitous and present in many other materials with two cations as well. Depending on the energy level of cation vacancies in a specific material, this can lead to either strongly insulating or conducting states which are very robust against impurities and independent of doping or oxygen partial pressure. This may either impede an adjustment of the intended conductivity, or, if the Fermi level is pinned at a desired level, guard against detrimental effects of impurities.

5. Experimental Section

Sample Preparation: Various $SrTiO_3$ powders were prepared via a mixed oxide route, starting with $SrCO_3$, TiO_2 , and depending on the dopant, Fe_2O_3 , NiO , or Al_2O_3 (Sigma Aldrich, Germany). Stoichiometric amounts of the respective materials were weighed and then mixed for at least 40 min in an agate mortar. Subsequently, the pressed powders were calcined at $1000\text{ }^\circ\text{C}$ for 2h in ambient air. After an additional milling step, the powders were pressed at 3kbar using a cold isostatic press and subsequently sintered at $1200\text{ }^\circ\text{C}$ for 5h in air. XRD measurements confirmed the phase purity of the obtained pellets. Those were used as targets for pulsed laser deposition. A summary of all targets is given in Table 1. Different substrates, namely undoped $SrTiO_3$ (CrysTec GmbH,

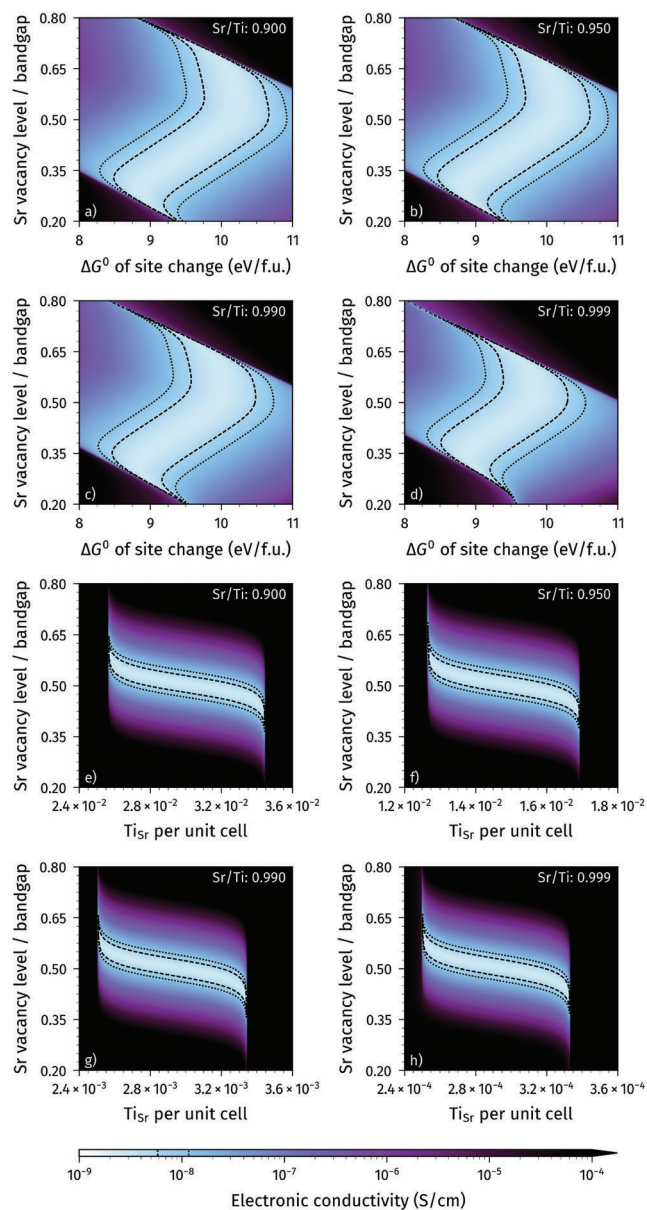


Figure 11. a) to d) Contour plots of the electronic conductivity at 400 °C, $p_{O_2} = 1$ bar for undoped SrTiO₃ thin films of different Sr/Ti ratios for different V_{Sr} levels in the band gap and different standard Gibbs free energies of the site change reaction ΔG^0 . The inner bold dashed lines indicate the region in which the conductivity is less than a factor of two above the intrinsic conductivity (i.e. for $[e^-] = [h^*]$), the outer dashed lines indicate a factor of four. The calculations are done in two steps: First, the equilibrium Ti_{Sr} concentration is calculated under PLD conditions (650 °C, 0.15 mbar O_2). Then, the Ti_{Sr} concentration is taken as frozen-in and all other defect concentrations are recalculated for 400 °C. Sr vacancies around mid-gap and ΔG^0 around 10 eV cause pseudo-intrinsic behavior for a very broad range of Sr/Ti ratios. e) to h) Contour plots indicating the electronic conductivity at 400 °C, $p_{O_2} = 1$ bar for an undoped SrTiO₃ thin film with different Sr/Ti ratios, for V_{Sr} levels varying around mid-gap and different Ti_{Sr} fractions. The solid lines indicate the region in which the conductivity is less than a factor of two above the intrinsic conductivity (i.e. for $[e^-] = [h^*]$), dashed lines indicate a factor of four. It is seen that the tolerance of pseudo-intrinsic behavior with respect to the Ti_{Sr} ratio strongly decreases when the V_{Sr} electronic level deviates significantly from mid-gap.

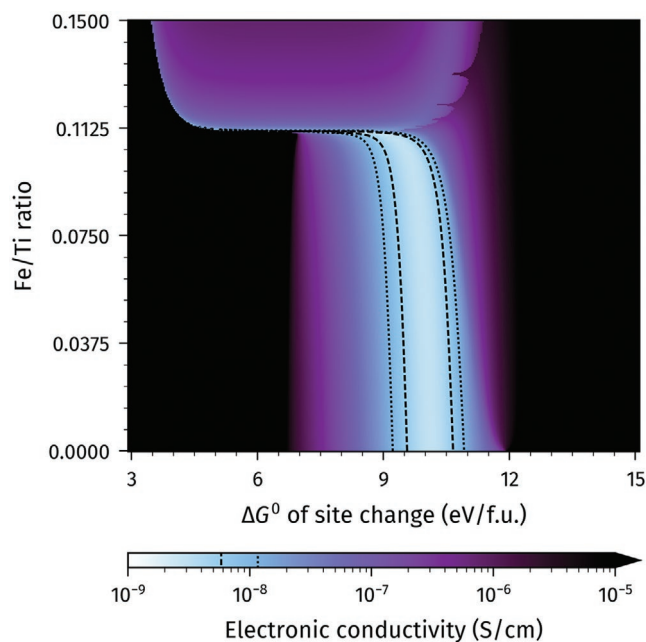


Figure 12. Electronic conductivities at 400 °C, $p_{O_2} = 1$ bar, compared to the intrinsic conductivity for different ΔG^0 values, Sr vacancies being exactly mid-gap and the Fe doping level varying while Sr/(Fe+Ti) is fixed at 0.90 and Fe_{Sr} is neglected here. In a broad range of Fe doping levels the pseudo-intrinsic situation again results as long as ΔG^0 is between 9.5 and 10.5 eV.

Germany), Nb-doped SrTiO₃ single crystals (0.5% wt Nb content, CrysTec GmbH, Germany) and yttria stabilized zirconia (YSZ, 9.5mol% Y₂O₃, CrysTec GmbH, Germany), all (001) oriented, were used in this study. For conductivity measurements, Nb-doped SrTiO₃ was used as a substrate due to its high conductivity. Thereby, the across-plane conductivity (or resistance) of the different thin films can be measured. In addition, the good match of the lattice parameter between undoped or slightly doped SrTiO₃ and the Nb:SrTiO₃ substrate leads to an epitaxial growth of the thin films. For this very reason, undoped SrTiO₃ substrates were used for XRD measurements and reciprocal space mapping. STO films for electrical characterization (grown on Nb:STO) and for XRD (grown on STO) were assumed to be identical in their chemical, crystallographic, and electrical properties. For the chemical analysis, YSZ was used as a substrate. In this case, no epitaxial growth takes place, but the chemical composition of these films should still correspond to that of films used for electrical characterization and XRD. The YSZ substrates did not contain significant impurities from elements relevant for the SrTiO₃ thin films (Sr, Ti, Fe, Ni, Al) and were therefore highly suitable for elemental analysis.

SrTiO₃ based thin films (undoped and acceptor doped) were prepared by pulsed laser deposition using a KrF excimer laser ($\lambda = 248$ nm) (COMPex Pro 201F, Coherent, Netherlands) with pulse duration of 25 ns. For the deposition process, a pulse frequency of 5Hz, a laser fluence of 1.1 J cm⁻², a substrate-target distance of 55 mm, an oxygen pressure of 0.15 mbar and a substrate temperature of 650 °C were set. Thin films with different thicknesses from 80 to 350 nm were investigated.

Circular Pt thin film micro-electrodes were prepared on top of the SrTiO₃ thin films. The corresponding Pt thin films were sputter-deposited in a high voltage magnetron coating device (BAL-TEC MED 020, Germany) and subsequently micro-patterned by lift-off photolithography. Only the 0.4% Fe-doped SrTiO₃ film has La_{0.6}Sr_{0.4}CoO_{3- δ} microelectrodes, prepared as described in ref. [106] for better comparison with literature. The micro-electrodes were contacted with Pt needles during impedance measurements. A schematic representation of the sample design is given in **Figure 13**.

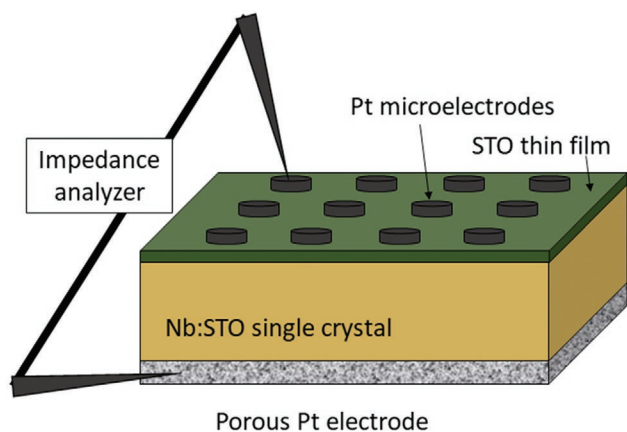


Figure 13. Sketch of a typical sample for electrochemical characterization with a (doped or nominally undoped) SrTiO₃ thin film on a Nb-doped SrTiO₃ substrate. For well-defined electrical contact, circular Pt microelectrodes (300 μm in diameter) are deposited on top of the SrTiO₃ thin film. A porous Pt layer acts as the counter electrode at the bottom of the Nb-doped SrTiO₃ single crystal.

Impedance Spectroscopy: In order to investigate the conductivity of the thin films, electrochemical impedance spectroscopy (EIS) with an Alpha-A High Resolution Analyzer (Novocontrol, Germany) was used. For temperature control, all electrochemical measurements were performed in a homogeneously heated furnace described in ref. [107] within a temperature range of 280 to 740 °C. The impedance was probed in a frequency range from 0.9 MHz to 1 Hz with a resolution of 10 points per decade, using an AC rms amplitude of 20 mV.

Chemical Analysis: First, the thin films on YSZ were dissolved in 3% v/v HNO₃ and 0.3% v/v HF for 30 min at 25 °C and the obtained solution was subsequently analyzed via solution based ICP-OES (iCAP 6500, Thermo Fisher Scientific, USA). For quantification, liquid standard solutions were used for external calibration. For more details, see Section S1, Supporting Information.

For comparison, the Sr/Ti ratio of nominally 5% Fe-doped SrTiO₃ was investigated using RBS. Experiments were performed at the ETH Tandatron accelerator using a 2 MeV He beam. Back-scattered particles were detected by a silicon PIN diode under 168° and data were analyzed by comparison with RUMP simulations.^[108] The Fe/Ti ratio was subsequently investigated using time-of-flight heavy ion elastic recoil detection analysis (ToF-ERDA). 13 MeV ¹²⁷I was employed as primary beam and recoiling sample atoms were analyzed by the combination of a ToF-spectrometer with a gas ionization detector.^[109] Biparametric data were converted to mass spectra and analyzed using a custom software.

X-Ray Diffraction: In order to investigate the lattice mismatch between deposited SrTiO₃ thin films and the nominally undoped (001) oriented SrTiO₃ substrates, reciprocal space maps of the (002), (103), and (113) reflections were recorded. The measurements were conducted on an Empyrean multipurpose diffractometer (Malvern Panalytical Ltd, UK) with a Cu-anode operating at 45 kV and 40 mA, which yielded a wavelength of λ = 1.5406 Å (Cu K_{α1} radiation) and λ = 1.5444 Å (Cu K_{α2} radiation). A hybrid monochromator (2 × Ge(220)) with a 1/32 divergence slit and a 4 mm mask was placed in the incident X-ray beam. A GaliPIX 3D detector was used in the frame-based mode. This specific detector adjustment allowed to measure 6.867° in 2θ without moving the GaliPIX with a resolution of 0.014°. The need of only scanning ω with a step size of 0.007° reduced the required time for data acquisition tremendously. Reciprocal space maps were measured for the (002) (ω = 23.238°, 2θ = 46.475°), the (103) (ω = 20.138°, 2θ = 46.475°), and the (113) (ω = 15.600°, 2θ = 46.475°) reflections. The (103) and (113) reflections also depended on the angle φ. In order to optimize the obtained signals, φ had to be adjusted before each measurement (rotation along the axis perpendicular to the sample surfaces). In total four different thin

films (from nominally undoped, 0.4% Ni-doped, 0.3% Al-doped, and 1% Fe-doped SrTiO₃ targets) deposited on undoped SrTiO₃ single crystals were measured at ambient conditions.

Positron Annihilation Lifetime Spectroscopy: Variable energy positron annihilation lifetime spectroscopy measurements were conducted on nominally undoped SrTiO₃ and Fe-doped SrTiO₃ single crystals as well as thin films at the mono-energetic positron source beamline at Helmholtz-Zentrum Dresden-Rossendorf, Germany.^[110] A digital lifetime CrBr₃ scintillator detector (51 mm diameter and 25.4 mm length) coupled to a Hamamatsu R13089-100 PMT was used. The detector was μ-metal shielded and housed inside a solid Au casing. For data acquisition, a multi-channel digitizer (SPDevices ADQ14DC-2X) with 14-bit vertical resolution and 2 GS/s horizontal resolution was utilized. Time resolution down to ≈0.210 ns was achieved. Typically, a lifetime spectrum $N(t)$ is described by $N(t) = \sum \tau_i^{-1} I_i \exp(t/\tau_i)$, where τ_i and I_i are the positron lifetime and intensity of the i th component, respectively ($\sum I_i = 1$) and convoluted with two Gaussian functions with distinct shifts and intensities.

All spectra contained at least 10⁷ counts and were decomposed using the nonlinear least-square based package PALSfit fitting software^[111] into two or three discrete lifetime components, which directly evidence delocalized bulk annihilation (τ_B) and localized annihilation at two different defect types (sizes; τ_1, τ_2). The corresponding relative intensities reflected to a large extent the concentration of each defect type (size) as long as the size of the compared defects is within a similar range. In general, the positron lifetime scaled directly with defect size. The larger the open volume, the longer positrons will live due to reduced electron density.^[112] The positron lifetime and its intensity were probed as a function of positron implantation energy E_p , which was proportional to the positron implantation depth.

XSW Measurements: The XSW technique is a method allowing direct structure determination with pm resolution.^[113] Such measurements were conducted at the chemical crystallography beamline P24 at the PETRA III storage ring at Deutsches Elektronen-Synchrotron (DESY) in Hamburg, Germany. The standing wave field was generated by interference of the incoming beam and the Bragg reflected beam from a Fe-doped SrTiO₃ thin film (deposited on an SrTiO₃ single crystal). Photoabsorption and, as a result, also emission of fluorescence from the probed atoms were proportional (within electric-dipole approximation) to the intensity of the interference field at the respective atoms. Atoms located at the maxima of the standing wave emitted more fluorescence whereas atoms at positions of the destructive interference emitted less. By changing incident angle or the photon energy, the position of the nodes and anti-nodes of the interference field can be varied, resulting in changes of the fluorescence yield. For different atom positions (e.g., interstitial, A, and/or B site) different dependencies from the deviation of the Bragg angle can be observed. Here, the angular dependency of the Fe K-fluorescence yield was measured.

To investigate whether Fe was located at a lattice site (A-site and B-site) or at an interstitial site, the (002) reflection was probed. To distinguish between A- and B-site occupancy of Fe, the (001) or (003) reflection can be used. At the (003) reflection, the probed sample volume was smaller, thus minimizing the potential influence of spatial variation of the substrate (e.g., due to substrate imperfections). Rocking scans of the (002) and (003) reflections were carried out on 220 nm thick Fe-doped SrTiO₃ thin films deposited from PLD targets with a stoichiometric composition of Sr_{1.00}Ti_{0.98}Fe_{0.02}O₃ as well as a 5% Sr overstoichiometry (Sr_{1.05}Ti_{0.98}Fe_{0.02}O₃) to compensate Sr loss in the preparation process.^[60] All XSW experiments were carried out at ambient conditions. For all measurements, an incident beam energy of 8.5 keV was used, corresponding to a wavelength of 1.4586 Å. The sample was oriented to fulfill the Bragg condition, and rocking scans around this position were performed.

A fluorescence spectrum was recorded at each angular step of the scan. Fluorescence spectra from several scans were summed up in order to improve the counting statistics. Then the chosen spectral line was fitted with a Gaussian function and linear background, and the yield calculated as an integral of the Gaussian. Subsequently, the obtained

results were compared to simulations for different Fe occupancies (A-site, B-site, mixed, interstitial). The simulations were based on the dynamical theory of diffraction,^[14] assuming a finite crystal thickness, so that the influence of the wave fields related to both branches of the dispersion surface was taken into account.

X-Ray Absorption Spectroscopy: XAS was performed at the surfaces/interfaces: microscopy beamline at the Swiss light source, Paul Scherrer Institute (PSI), Switzerland. The absorption of linear polarized X-rays was measured in energy ranges of 521.0–589.0 eV (O K-edge), 441.0–479.0 eV (Ti L_{2,3}-edge), and 691.1–749.0 eV (Fe L_{2,3}-edge) at room temperature. At least four different positions were probed on each sample. Here, 220 nm thick thin films deposited from a SrTiO₃ target with 2% Fe, were used directly after deposition (as-deposited) and after subsequent annealing for 12h at 700 °C in air. For these samples, the total electron yield as well as the fluorescence yield were measured, with the fluorescence mode being more bulk sensitive^[15] while the information depth of total electron yield measurements was in the range of several nanometers,^[15–17] comparable to the width of space charge layers.^[5] The obtained spectra were normalized to the incident beam intensity using a gold mesh and processed using the Athena program.^[18] Interpretation of the XAS spectra was supported by linear combinations of simulated spectra of Fe in different oxidation state, that is, Fe²⁺ and Fe³⁺, in octahedral geometry using TM4XAS.^[19]

Supporting Information

Supporting Information is available from the Wiley Online Library or from the author.

Acknowledgements

The authors like to acknowledge the financial support and open access funding provided by the Austrian Science Fund (FWF) (F4509–N16) and funding from the European Union's Horizon 2020 research and innovation program under grant agreement No. 824072 (Harvestore). PALS measurements were carried out at ELBE at the Helmholtz-Zentrum Dresden - Rossendorf e.V., and XSW measurements were performed at Deutsches Elektronen-Synchrotron DESY, members of the Helmholtz Association. The authors would like to thank facility staff at ELBE (Ahmed G. Attallah, Eric Hirschmann) for assistance. Part of this work was carried out at the Swiss Light Source, Paul Scherrer Institut (Switzerland) and ETH Zürich.

Conflict of Interest

The authors declare no conflict of interest.

Data Availability Statement

The data that support the findings of this study are available from the corresponding author upon reasonable request.

Keywords

fermi level pinning, pulsed laser depositions, site occupations, Sr vacancies, SrTiO₃ thin films, strontium titanate, thin film characterization, ultra-low conductivities

Received: February 24, 2022

Revised: May 19, 2022

Published online: July 7, 2022

- [1] I. Denk, W. Münch, J. Maier, *J. Am. Ceram. Soc.* **1995**, *78*, 3265.
- [2] R. Moos, K. H. Hardtl, *J. Am. Ceram. Soc.* **1997**, *80*, 2549.
- [3] R. A. De Souza, J. Fleig, R. Merkle, J. Maier, *Metallkd.* **2003**, *94*, 218.
- [4] A. Rothschild, W. Menesklou, H. L. Tuller, E. Ivers-Tiffée, *Chem. Mater.* **2006**, *18*, 3651.
- [5] C. Ohly, S. Hoffmann-Eifert, X. Guo, J. Schubert, R. Waser, *J. Am. Ceram. Soc.* **2006**, *89*, 2845.
- [6] J. Wang, T. Fang, S. Yan, Z. Li, T. Yu, Z. Zou, *Comput. Mater. Sci.* **2013**, *79*, 87.
- [7] S. Tonda, S. Kumar, O. Anjaneyulu, V. Shanker, *Phys. Chem. Chem. Phys.* **2014**, *16*, 23819.
- [8] R. A. Maier, A. C. Johnston-Peck, M. P. Donohue, *Adv. Funct. Mater.* **2016**, *26*, 8325.
- [9] M. J. Akhtar, Z. U. N. Akhtar, R. A. Jackson, C. R. A. Catlow, *J. Am. Ceram. Soc.* **1995**, *78*, 421.
- [10] D. Wang, J. Ye, T. Kako, T. Kimura, *J. Phys. Chem. B* **2006**, *110*, 15824.
- [11] J. Shi, J. Ye, L. Ma, S. Ouyang, D. Jing, L. Guo, *Chem. - Eur. J.* **2012**, *18*, 7543.
- [12] O. Okhay, A. Wu, P. M. Vilarinho, A. Tkach, *Appl. Phys. Lett.* **2010**, *96*, 152906.
- [13] U. S. Shenoy, H. Bantawal, D. K. Bhat, *J. Phys. Chem. C* **2018**, *122*, 27567.
- [14] U. S. Shenoy, D. K. Bhat, *J. Phys. Chem. Solids* **2021**, *148*, 109708.
- [15] M. Choi, F. Oba, I. Tanaka, *Phys. Rev. Lett.* **2009**, *103*, 185502.
- [16] A. Karjalainen, V. Prozhveeva, I. Makkonen, C. Guguschev, T. Markurt, M. Bickermann, F. Tuomisto, *J. Appl. Phys.* **2020**, *127*, 245702.
- [17] B. Liu, V. R. Cooper, H. Xu, H. Xiao, Y. Zhang, W. J. Weber, *Phys. Chem. Chem. Phys.* **2014**, *16*, 15590.
- [18] H. Lu, D. Lee, K. Klyukin, L. Tao, B. Wang, H. Lee, J. Lee, T. R. Paudel, L.-Q. Chen, E. Y. Tsybmal, V. Alexandrov, C.-B. Eom, A. Gruverman, *Nano Lett.* **2018**, *18*, 491.
- [19] U. N. Gries, M. Kessel, F. V. E. Hensling, R. Dittmann, M. Martin, R. A. De Souza, *Phys. Rev. Mater.* **2020**, *4*, 123404.
- [20] A. Walsh, C. R. A. Catlow, A. G. H. Smith, A. A. Sokol, S. M. Woodley, *Phys. Rev. B* **2011**, *83*, 220301.
- [21] J. P. Parras, A. R. Genreith-Schriever, H. Zhang, M. T. Elm, T. Norby, R. A. De Souza, *Phys. Chem. Chem. Phys.* **2018**, *20*, 8008.
- [22] Y. Li, S. N. Phattalung, S. Limpijumngong, J. Kim, Y. J., *Phys. Rev. B* **2011**, *84*, 245307.
- [23] A. Kalabukhov, R. Gunnarsson, J. Börjesson, E. Olsson, T. Claesson, D. Winkler, *Phys. Rev. B* **2007**, *75*, 121404.
- [24] F. S. Oliveira, A. C. Favero, S. T. Renosto, M. S. de Luz, C. A. M. dos Santos, *Mater. Res.* **2018**, *21*, e20170887.
- [25] F. Azough, S. S. Jackson, D. Ekren, R. Freer, M. Molinari, S. R. Yeandel, P. M. Panchmatia, S. C. Parker, D. H. Maldonado, D. M. Kepaptsoglou, Q. M. Ramasse, *ACS Appl. Mater. Interfaces* **2017**, *9*, 41988.
- [26] V. Vonk, J. Huijben, D. Kukuruznyak, A. Stierle, H. Hilgenkamp, A. Brinkman, S. Harkema, *Phys. Rev. B* **2012**, *85*, 045401.
- [27] K. Fukushima, S. Shibagaki, *Thin Solid Films* **1998**, *315*, 238.
- [28] R. Groenen, J. Smit, K. Orsel, A. Vailionis, B. Bastiaens, M. Huijben, K. Boller, G. Rijnders, G. Koster, *APL Mater.* **2015**, *3*, 070701.
- [29] D. J. Keeble, S. Wicklein, L. Jin, C. L. Jia, W. Egger, R. Dittmann, *Phys. Rev. B* **2013**, *87*, 195409.
- [30] T. Ohnishi, M. Lippmaa, T. Yamamoto, S. Meguro, H. Koinuma, *Appl. Phys. Lett.* **2005**, *87*, 241919.
- [31] T. Ohnishi, T. Yamamoto, S. Meguro, H. Koinuma, M. Lippmaa, *J. Phys.: Conf. Ser.* **2007**, *59*, 514.
- [32] T. Ohnishi, K. Shibuya, T. Yamamoto, M. Lippmaa, *J. Appl. Phys.* **2008**, *103*, 103703.

- [33] K. Orsel, R. Groenen, B. Bastiaens, G. Koster, G. Rijnders, K.-J. Boller, *APL Mater.* **2015**, 3, 106103.
- [34] Y. Tokuda, S. Kobayashi, T. Ohnishi, T. Mizoguchi, N. Shibata, Y. Ikuhara, T. Yamamoto, *Appl. Phys. Lett.* **2011**, 99, 033110.
- [35] S. Wicklein, A. Sambri, S. Amoroso, X. Wang, R. Bruzzese, A. Koehl, R. Dittmann, *Appl. Phys. Lett.* **2012**, 101, 131601.
- [36] C. Xu, S. Wicklein, A. Sambri, S. Amoroso, M. Moors, R. Dittmann, *J. Phys. D: Appl. Phys.* **2013**, 47, 034009.
- [37] M. Kubicek, S. Taibl, E. Navickas, H. Hutter, G. Faflek, F. J., *J. Electroceram.* **2017**, 39, 197.
- [38] C. Funck, C. Bäumer, S. Wiefels, T. Hennen, R. Waser, S. Hoffmann-Eifert, R. Dittmann, S. Menzel, *Phys. Rev. B* **2020**, 102, 035307.
- [39] C. Lenser, A. Koehl, I. Slipukhina, H. Du, M. Patt, V. Feyrer, C. M. Schneider, M. Lezaic, R. Waser, R. Dittmann, *Adv. Funct. Mater.* **2015**, 25, 6360.
- [40] N. Raab, C. Bäumer, R. Dittmann, *AIP Adv.* **2015**, 5, 047150.
- [41] M. Xuejiang, C. H. Chan, R. YingyueWang, J. JianboWang, X. Qiu, *Appl. Phys. Lett.* **2020**, 116, 102101.
- [42] E. Sediva, W. J. Bowman, J. C. Gonzalez-Rosillo, J. L. M. Rupp, *Adv. Electron. Mater.* **2019**, 5, 1800566.
- [43] D.-H. Kwon, S. Lee, C. S. Kang, Y. S. Choi, S. J. Kang, H. L. Cho, W. Sohn, J. Jo, S.-Y. Lee, K. H. Oh, T. W. Noh, R. A. de Souza, M. Martin, M. Kim, *Adv. Mater.* **2019**, 31, 1901322.
- [44] K. Szot, R. Dittmann, W. Speier, R. Waser, *Phys. Status Solidi RRL* **2007**, 1, 86.
- [45] R. Merkle, R. A. De Souza, J. Maier, *Angew. Chem., Int. Ed.* **2001**, 40, 2126.
- [46] A. Viernstein, M. Kubicek, M. Morgenbesser, G. Walch, G. C. Brunauer, J. Fleig, *Adv. Funct. Mater.* **2019**, 29, 1900196.
- [47] G. C. Brunauer, B. Rotter, G. Walch, E. Esmaeili, A. K. Opitz, K. Ponweiser, J. Summhammer, F. J., *Adv. Funct. Mater.* **2016**, 26, 120.
- [48] M. Siebenhofer, T. Huber, W. Artner, J. Fleig, M. Kubicek, *Acta Mater.* **2021**, 203, 116461.
- [49] F. V. E. Hensling, D. J. Keeble, J. Zhu, S. Brose, C. Xu, F. Gunkel, S. Danylyuk, S. S. Nonnenmann, W. Egger, R. Dittmann, *Sci. Rep.* **2018**, 8, 8846.
- [50] G. Walch, B. Rotter, G. C. Brunauer, E. Esmaeili, A. K. Opitz, M. Kubicek, J. Summhammer, K. Ponweiser, F. J., *J. Mater. Chem. A* **2017**, 5, 1637.
- [51] A. Senocrate, E. Kotomin, J. Maier, *Helv. Chim. Acta* **2020**, 103, e2000073.
- [52] S. Taibl, G. Faflek, J. Fleig, *Nanoscale* **2016**, 8, 13954.
- [53] C. Ohly, S. Hoffmann-Eifert, K. Szot, R. Waser, *J. Eur. Ceram. Soc.* **2001**, 21, 1673.
- [54] Y.-T. Chi, M. Youssef, L. Sun, K. J. Van Vliet, B. Yildiz, *Phys. Rev. Mater.* **2018**, 2, 055801.
- [55] L. Iglesias, A. Sarantopoulos, C. Magén, F. Rivadulla, *Phys. Rev. B* **2017**, 95, 165138.
- [56] A. Vaillionis, H. Boschker, W. Siemons, E. P. Houwman, D. H. A. Blank, G. Rijnders, G. Koster, *Phys. Rev. B* **2011**, 83, 064101.
- [57] A. Koehl, D. Kajewski, J. Kubacki, C. Lenser, R. Dittmann, P. Meuffels, K. Szot, R. Waser, J. Szade, *Phys. Chem. Chem. Phys.* **2013**, 15, 8311.
- [58] D. J. Keeble, S. Wicklein, R. Dittmann, L. Ravelli, R. A. Mackie, W. Egger, *Phys. Rev. Lett.* **2010**, 105, 226102.
- [59] M. L. Reinle-Schmitt, C. Cancellieri, A. Cavallaro, G. F. Harrington, S. J. Leake, E. Pomjakushina, J. A. Kilner, P. R. Willmott, *Nanoscale* **2014**, 6, 2598.
- [60] M. Morgenbesser, S. Taibl, M. Kubicek, A. Schmid, A. Viernstein, N. Bodenmüller, C. Herzig, F. Baiutti, J. de Dios Sirvent, M. O. Liedke, M. Butterling, A. Wagner, W. Artner, A. Limbeck, A. Tarancon, J. Fleig, *Nanoscale Adv.* **2021**, 3, 6114.
- [61] J. Jamnik, J. Maier, *J. Electrochem. Soc.* **1999**, 146, 4183.
- [62] J. Jamnik, J. Maier, S. Pejovnik, *Electrochim. Acta* **1999**, 44, 4139.
- [63] J. Jamnik, J. Maier, *Phys. Chem. Chem. Phys.* **2001**, 3, 1668.
- [64] S. Rodewald, J. Fleig, J. Maier, *J. Eur. Ceram. Soc.* **2001**, 21, 1749.
- [65] J. Schou, *Appl. Surf. Sci.* **2009**, 255, 5191.
- [66] S. Amoroso, A. Sambri, X. Wang, *J. Appl. Phys.* **2006**, 100, 013302.
- [67] A. Ojeda-G-P, M. Döbeli, T. Lippert, *Adv. Mater. Interfaces* **2018**, 5, 1701062.
- [68] J. Chen, M. Döbeli, D. Stender, K. Conder, A. Wokaun, C. W. Schneider, T. Lippert, *Appl. Phys. Lett.* **2014**, 105, 114104.
- [69] H. Hu, F. Shao, J. Chen, M. Döbeli, Q. Song, Q. Zhang, D. Zhao, J. Miao, X. Xu, Y. Jiang, *Ceram. Int.* **2019**, 45, 13138.
- [70] S. Kobayashi, Y. Tokuda, T. Ohnishi, T. Mizoguchi, N. Shibata, Y. Sato, Y. Ikuhara, T. Yamamoto, *J. Mater. Sci.* **2011**, 46, 4354.
- [71] M. Morgenbesser, S. Taibl, M. Kubicek, A. Schmid, A. Viernstein, N. Bodenmüller, C. Herzig, F. Baiutti, J. de Dios Sirvent, M. O. Liedke, M. Butterling, A. Wagner, W. Artner, A. Limbeck, A. Tarancon, J. Fleig, *Nanoscale Adv.* **2021**, 3, 6114.
- [72] R. Loetzsch, A. Lübcke, I. Uschmann, E. Förster, V. Große, M. Thuerk, T. Koettig, F. Schmidl, P. Seidel, *Appl. Phys. Lett.* **2010**, 96, 071901.
- [73] S. A. Hayward, E. K. H. Salje, *Phase Transitions* **1999**, 68, 501.
- [74] M. A. McCoy, R. W. Grimes, W. E. Lee, *Philos. Mag. A* **1997**, 75, 833.
- [75] T. Suzuki, Y. Nishi, M. Fujimoto, *Philos. Mag. A* **2000**, 80, 621.
- [76] E. J. Tarsa, E. A. Hachfeld, F. T. Quinlan, J. S. Speck, M. Eddy, *Appl. Phys. Lett.* **1996**, 68, 490.
- [77] Q. Y. Lei, G. Z. Liu, X. X. Xi, *Integr. Ferroelectr.* **2013**, 141, 128.
- [78] C. M. Brooks, L. F. Kourkoutis, T. Heeg, J. Schubert, D. A. Muller, D. G. Schlom, *Appl. Phys. Lett.* **2009**, 94, 162905.
- [79] M. Markovich, J. Roqueta, J. Santiso, E. Lakin, E. Zolotoyabko, A. Rothschild, *Appl. Surf. Sci.* **2012**, 258, 9496.
- [80] M. Siebenhofer, F. Baiutti, J. Dios Sirvent, T. M. Huber, A. Viernstein, S. Smetaczek, C. Herzig, M. O. Liedke, M. Butterling, A. Wagner, E. Hirschmann, A. Limbeck, A. Tarancon, J. Fleig, M. Kubicek, *J. Eur. Ceram. Soc.* **2021**, 42, 1510.
- [81] R. A. Maier, E. Cockayne, M. Donohue, G. Cibin, I. Levin, *Chem. Mater.* **2020**, 32, 4651.
- [82] F. M. F. Groot, J. Faber, J. J. M. Michiels, M. T. Czyżyk, M. Abbate, J. C. Fuggle, *Phys. Rev. B* **1993**, 48, 2074.
- [83] Q. Zhao, X.-L. Cheng, *J. Phys. Chem. A* **2020**, 124, 322.
- [84] J. Kubacki, D. Kajewski, A. Koehl, M. Wojtyniak, R. Dittmann, J. Szade, *Radiat. Phys. Chem.* **2013**, 93, 123.
- [85] J. Schlappa, C. F. Chang, Z. Hu, E. Schierle, H. Ott, E. Weschke, G. Kaindl, M. Huijben, G. Rijnders, D. H. A. Blank, L. H. Tjeng, C. Schüßler-Langeheine, *J. Phys.: Condens. Matter* **2011**, 24, 035501.
- [86] R. Zucca, *J. Appl. Phys.* **1977**, 48, 1987.
- [87] N. Osawa, R. Takahashi, M. Lippmaa, *Appl. Phys. Lett.* **2017**, 110, 263902.
- [88] V. V. Laguta, I. V. Kondakova, I. P. Bykov, M. D. Glinchuk, A. Tkach, P. M. Vilarinho, L. Jastrabik, *Phys. Rev. B* **2007**, 76, 054104.
- [89] M. Valant, T. Kolodiazhnyi, I. Arçon, F. Aguesse, A.-K. Axelsson, N. M. Alford, *Adv. Funct. Mater.* **2012**, 22, 2114.
- [90] A. Tkach, P. M. Vilarinho, D. Nuzhnyy, J. Petzelt, *Acta Mater.* **2010**, 58, 577.
- [91] D. Lu, Y. Zheng, L. Yuan, *Materials* **2019**, 12, 1525.
- [92] P. Serna-Gallén, H. Beltrán-Mir, E. Cordoncillo, A. R. West, R. Balda, J. Fernández, *J. Mater. Chem. C* **2019**, 7, 13976.
- [93] J. H. Kim, S. H. Yoon, Y. H. Han, *J. Eur. Ceram. Soc.* **2007**, 27, 1113.
- [94] R. A. Maier, K. F. Garrity, A. Ozarowski, M. P. Donohue, G. Cibin, I. Levin, *Acta Mater.* **2021**, 207, 116688.
- [95] P. B. Groszewicz, L. Koch, S. Steiner, A. Ayrikyan, K. G. Webber, T. Frömling, K. Albe, G. Buntkowsky, *J. Mater. Chem. A* **2020**, 8, 18188.
- [96] K. Klyukin, V. Alexandrov, *Phys. Rev. B* **2017**, 95, 035301.
- [97] R. A. De Souza, *Adv. Funct. Mater.* **2015**, 25, 6326.

- [98] A. S. Tang, J. Pellicciari, Q. Song, Q. Song, S. Ning, J. W. Freeland, R. Comin, C. A. Ross, *Phys. Rev. Mater.* **2019**, *3*, 054408.
- [99] R. Merkle, J. Maier, *Phys. Chem. Chem. Phys.* **2003**, *5*, 2297.
- [100] M. Saiful Islam, *J. Mater. Chem.* **2000**, *10*, 1027.
- [101] N. Kuganathan, F. Baiutti, A. Tarancón, J. Fleig, A. Chroneos, *Solid State Ionics* **2021**, *361*, 115570.
- [102] R. A. Maier, C. A. Randall, *J. Am. Ceram. Soc.* **2016**, *99*, 3350.
- [103] F. V. E. Hensling, C. Xu, F. Gunkel, R. Dittmann, *Sci. Rep.* **2017**, *7*, 39953.
- [104] M. J. Akhtar, Z.-U.-N. Akhtar, R. A. Jackson, C. R. A. Catlow, *J. Am. Ceram. Soc.* **1995**, *78*, 2421.
- [105] T. Tanaka, K. Matsunaga, Y. Ikuhara, T. Yamamoto, *Phys. Rev. B* **2003**, *68*, 205213.
- [106] M. Kubicek, A. Limbeck, T. Frömling, H. Hutter, J. Fleig, *J. Electrochem. Soc.* **2011**, *158*, 727.
- [107] T. M. Huber, A. K. Opitz, M. Kubicek, H. Hutter, J. Fleig, *Solid State Ionics* **2014**, *268*, 82.
- [108] L. R. Doolittle, *Nucl. Instr. Methods Phys. Res., B* **1986**, *15*, 227.
- [109] C. Kottler, M. Döbeli, F. Glaus, M. Suter, *Nucl. Instrum. Methods Phys. Res., Sect. B: Beam Interact. Mater. Atoms* **2006**, *248*, 155.
- [110] A. Wagner, M. Butterling, M. O. Liedke, K. Potzger, R. Krause-Rehberg, *AIP Conf. Proc.* **2018**, *1970*, 040003.
- [111] J. V. Olsen, P. Kirkegaard, N. J. Pedersen, M. Eldrup, *Phys. Status Solidi C* **2007**, *4*, 4004.
- [112] F. Tuomisto, I. Makkonen, *Rev. Mod. Phys.* **2013**, *85*, 1583.
- [113] J. Zegenhagen, A. Kazimirov, *The X-ray Standing Wave Technique: Principles and Applications*, World Scientific, Singapore **2013**.
- [114] A. Authier, in *International Tables for Crystallography Volume B: Reciprocal Space*, (Ed: U. Shmueli), Springer, Dordrecht **2001**, pp. 534–551.
- [115] S. Hayakawa, Y. Makiyama, T. Esumi, S. Qiao, A. Morikawa, S. Tohno, H. Namatame, T. Hirokawa, *AIP Conf. Proc.* **2007**, *882*, 869.
- [116] A. Ruosi, C. Raisch, A. Verna, R. Werner, B. A. Davidson, J. Fujii, R. Kleiner, D. Koelle, *Phys. Rev. B* **2014**, *90*, 125120.
- [117] J. S. Lee, Y. W. Xie, H. K. Sato, C. Bell, Y. Hikita, H. Y. Hwang, C. C. Kao, *Nat. Mater.* **2013**, *12*, 703.
- [118] B. Ravel, M. J. Newville, *J. Synchrotron Radiat.* **2005**, *12*, 4537.
- [119] E. Stavitski, F. M. Groot, *Micron* **2010**, *41*, 687.